https://doi.org/10.5194/egusphere-2026-3922
Preprint. Discussion started: 21 July 2026
© Author(s) 2026. CC BY 4.0 License.

Validation of high-resolution ICON-LES in complex terrain using observations from two HEFEX field campaigns

Alexander Georgi[1], Leopold Schlagbauer[2], Kristine Flacké Haualand[3], Malte Springer[1], Lindsey Nicholson[2], and Tobias Sauter[1]

[1]Humboldt-Universität zu Berlin, Germany
[2]Universität Innsbruck, Austria
[3]Western Norway University of Applied Sciences, Norway

Correspondence: Alexander Georgi (alexander.georgi.1@geo.hu-berlin.de)

Abstract. High-resolution atmospheric modeling in complex mountainous terrain remains challenging because multiscaleeterogeneity, thermally driven circulation, and multiscale interactions between local and synoptic forcing. In this study, we present an extensive validation of the high-resolution ICOsahedral Nonhydrostatic (ICON) model in glacierized alpine terrain using extensive observational data from two HinterEisFerner EXperiment (HEFEX) field campaigns conducted on the Hintereisferner glacier in Austria. By integrating a dense network of automatic weather stations, instrumented towers, Doppler wind lidars, and uncrewed aerial vehicle (UAV)-based vertical soundings, we evaluate the performance of ICON large-eddy simulations (LES) at a horizontal resolution of 51 m across a range of synoptic conditions and flow regimes. The model demonstrates good performance in reproducing near-surface temperature, humidity, and wind fields, as well as the vertical structure and temporal evolution of valley-scale atmospheric flows. The remaining biases in near-surface variables can largely be attributed to shallow stable boundary layer processes that remain unresolved even at this resolution. UAV and Doppler lidar observations further show that ICON captures the vertical thermodynamic structure and dominant diurnal evolution of glacier and valley wind systems well. Remaining discrepancies primarily occur during transition periods, particularly when multiple forcing mechanisms interact, where the model shows reduced skill in accurately representing the dominant flow direction and depth. Overall, these results demonstrate that ICON-LES is capable of realistically capturing three-dimensional atmospheric dynamics in complex mountainous terrain, providing a robust foundation for future investigations of atmosphere–cryosphere coupling and glacier–climate feedback in complex mountain environments.

1 Introduction

Mountains are recognized as generating some of the most dynamically complex meteorological conditions on Earth. Their highly variable topography results in complex interactions between synoptic-scale circulations and locally driven wind systems (Zardi and Whiteman, 2013; Oerlemans, 2010), leading to the formation of unique microclimates that can vary significantly over short distances. This complex interplay of atmospheric dynamics underscores the importance of understanding the mountain boundary layer (MBL) in greater detail. The MBL is the lowest part of the troposphere, directly influenced by mountainous terrain, where local topography and thermal effects strongly affect atmospheric flow and turbulence. The spatial heterogeneity

https://doi.org/10.5194/egusphere-2026-3922
Preprint. Discussion started: 21 July 2026
© Author(s) 2026. CC BY 4.0 License.

and rapid transitions between flow regimes within this layer make it fundamentally different from its flat-terrain counterpart (Lehner and Rotach, 2018). However, the thermally driven slope and valley winds and katabatic flows over glacier surfaces interact with larger-scale pressure gradients in ways that remain poorly understood. Therefore, advancing our knowledge of these interactions is vital for improving assessments of glacier responses to climatic changes, as these dynamic processes govern the exchange of heat, moisture, and momentum between the surface and atmosphere (Rotach et al., 2022), thereby directly impacting glacier mass balance (Hock, 2005).

Anthropogenic climate change is causing mountain glaciers to retreat worldwide. Changes in glacier geometry and surface properties not only transform the landscape but also modify surface–atmosphere exchange processes, specifically disrupting atmospheric–cryospheric coupling (e.g., Salerno et al., 2023). However, the extent of this coupling and its impact on local and regional climates remain insufficiently quantified. Gaining a better understanding of these coupling processes is crucial for identifying feedback mechanisms and understanding how energy and mass propagate across scales (e.g., Bugnard et al., 2025). Recent studies on smaller alpine glaciers have shown that katabatic flow, which previously decoupled near-surface temperatures over ice from ambient air temperatures, has weakened on retreating glaciers. At the same time, thermally induced up-valley flow intensifies, ultimately accelerating glacier melt (Shaw et al., 2025, 2023). More observations and process studies are needed to deepen our understanding of these interrelationships and improve projections of glacier evolution, hydrological resources, and regional climate responses (Salerno et al., 2023).

The harsh high-alpine environment imposes severe logistical constraints on in situ measurements (e.g., Haualand et al., 2025; Groos et al., 2025). Access is difficult, power supply is limited, and instrumentation deployed on ice or steep terrain is vulnerable to weather and instability issues. Consequently, field campaigns are sparse and predominantly rely on point measurements, capturing only a fraction of the spatial variability of the MBL (e.g., Sauter and Galos, 2016; Goger and Dipankar, 2024). The limited observational coverage impedes the ability to generalize the findings and evaluate numerical models under the full range of conditions encountered in complex terrain.

Numerical weather prediction (NWP) models are powerful tools for investigating atmospheric processes in mountain environments (e.g., Umek et al., 2021; Goger et al., 2022; Schmidli and Quimbayo-Duarte, 2023). When research utilizes these models at a sufficiently high resolution, they can explicitly resolve fine-scale flow features and generate continuous spatiotemporal fields beyond observational reach. Thus, NWP experiments can help close observational gaps, test hypotheses, and explore sensitivities to changing glacier states or atmospheric forcing (e.g., Haualand et al., 2025). However, decameter-scale modeling over complex terrain demands substantial computational resources, and the scarcity of observational datasets constrains rigorous model validation. Consequently, modelers must first demonstrate robust model performance before applying simulations to process studies, scenario testing, or atmosphere–cryosphere feedback investigations.

This study addresses a critical gap in the evaluation of high-resolution numerical models for complex mountain terrains. Previous validation studies have examined less complex terrain (Goger and Dipankar, 2024) or other established NWP systems, such as Weather Research and Forecasting (WRF; Goger et al., 2022). However, no equivalent assessment has been conducted on large-eddy simulations (LES) with the ICOsahedral Nonhydrostatic (ICON) model in glacierized high-alpine environments, although its triangular grid is well suited for steep topography (Zängl et al., 2015). To address this gap, we combined two

https://doi.org/10.5194/egusphere-2026-3922
Preprint. Discussion started: 21 July 2026
© Author(s) 2026. CC BY 4.0 License.

exceptional observational datasets collected on the Hintereisferner (HEF) glacier within the TEAMx international research program (Serafin et al., 2020) with high-resolution, real-case ICON-LES data. The observations include high-resolution in situ, uncrewed aerial vehicle (UAV), and remote-sensing measurements of near-surface conditions and glacier-valley circulation in the lowest hundreds of meters above ground across diverse meteorological regimes, a level of spatial and temporal coverage that is rare in remote glacierized environments (Nicholson et al., 2025). Together, these datasets and simulations form a robust framework for evaluating ICON's ability to represent complex flow structures, thermal regimes, and exchange processes that characterize high-mountain environments. This validation marks a necessary step toward applying such models to investigate key open questions in mountain climate research and advance our understanding of the changing atmosphere–cryosphere system, both regionally and globally.

2 Data and methods

2.1 Study site and field campaigns

The observational data for this study were collected during two coordinated measurement campaigns on the HEF, a valley glacier situated in the Rofen catchment of the Ötztal Alps in Austria. HEF is recognized as one of the world's long-term reference glaciers (WGMS, 2026) with glaciological observations dating back to the early 1950s (Kuhn et al., 1999; Strasser et al., 2018). In addition to long-term glaciological monitoring, the study area is supported by meteorological observations at high elevations. These extensive records have established HEF as a benchmark site for alpine glacier process studies. This study benefits from data collected by two permanent off-glacier automatic weather stations (AWSs), namely station Hintereis (STHE; 3 031 m ASL) and station Im Hinteren Eis (IHE; 3 260 m ASL), both operated by the University of Innsbruck (magenta triangles in Fig. 1; UIBK, 2026).

In 2022, the glacier spanned approximately 5.2 km^2, stretching from the 3 739 m summit of Weißkugel to a terminus at approximately 2 525 m above sea level (ASL). The glacier primarily faces northeast and features a broad, gently sloping ablation tongue that transitions into steeper cirque and icefall sections, with little or no remaining perennial accumulation area. The topography of the HEF promotes complex interactions between the glacier and valley winds. The gently inclined terrain supports persistent katabatic flows. Above, thermally driven valley winds, slope flow circulations, orographic flow, and mesoscale flow features such as mountain waves can be present. Data from a previous field campaign (Mott et al., 2020; Nicholson et al., 2025) demonstrated that such superimposed large-scale flows can significantly impact the glacier boundary layer, for example, through horizontal heat advection and ultimately by altering turbulent transport (Mott et al., 2020; Goger et al., 2022). These characteristics make the HEF a natural laboratory for studying glacier–atmosphere interactions and intricate boundary layer dynamics, providing an ideal environment for evaluating the performance of the ICON model in complex terrain.

The first campaign contributing to this study, HEFEX II (2nd HinterEisFerner EXperiment), was conducted from 15 August to 10 September 2023. This campaign primarily focused on near-surface atmospheric processes over glacier ice (Nicholson et al., 2025). An extensive network of 18 AWS was strategically deployed directly across the glacier surface. These stations

https://doi.org/10.5194/egusphere-2026-3922
Preprint. Discussion started: 21 July 2026
© Author(s) 2026. CC BY 4.0 License.

were arranged along the central flowline, complemented by two cross-glacier transects at 2 670 m and 2 750 m ASL (green triangles in Fig. 1). The stations were equipped with a variety of sensor configurations. All stations measured air temperature, while 14 stations additionally recorded wind speed and direction. Furthermore, ten stations were equipped with high-frequency ultrasonic anemometers for eddy covariance turbulence measurements. Two towers included measurement levels of up to 5 m, allowing for improved characterization of the shallow glacier boundary layer. This comprehensive setup proved invaluable for investigating both the spatial structure and temporal evolution of the glacier boundary layer, enabling a nuanced understanding of the microscale atmospheric dynamics that influence energy and mass exchanges at the ice surface during the ablation season.

The subsequent campaign, HEFEX III, conducted from 6 to 31 August 2025, extended the observational scope to integrate the valley atmosphere and the interactions between synoptic forcing, topographic influences, and katabatic flow. A 10 m tower (T272) was installed on the glacier at an elevation of 2 720 m ASL to monitor the near-surface flow conditions. This tower was equipped with five 3D ultrasonic anemometers at 0.5, 1, 3, 5, and 8.5 m, three 2D wind sensors at 2, 4, and 7 m, three air temperature and humidity sensors at 2, 5, and 7 m, and one gas analyzer at 1 m, providing detailed observations of turbulent exchange processes. Additional surface observations were provided by two off-glacier eddy covariance stations equipped with gas analyzers that were installed in the glacier forefield.

Two Doppler wind lidars, which measured continuously throughout the entire campaign, were used to assess valley-scale flow structures (red diamond in Fig. 1 inset). A HALO Photonics StreamLine XR system performed kilometer-range Plan Position Indicator (PPI) and Range–Height Indicator (RHI) scans, whereas a METEK WindRanger system conducted high-resolution measurements (PPI scans, 10° zenith angle) within the lowest 200 m above ground level (AGL). The RHI scans were oriented to capture the atmospheric flow structure both along the glacier flowline and across the valley.

HEFEX III also included two intensive observation periods (IOPs) from 6–10 August and 18–19 August. During these periods, a fleet of eight quadcopter UAVs (blue stars in Fig. 1 inset) and two fixed-wing UAVs conducted vertical soundings at 3 hour intervals up to 600 m AGL. The quadcopters ascended at 1 $\mathrm{m\,s^{-1}}$ and were equipped with iMet-XQ2 sensors at the front to maximize aspiration and minimize heat impact from the electronics (Kimball et al., 2020a). The sensors recorded meteorological measurements at 1 Hz to achieve a vertical resolution of 1 m. The iMet measurements from the UAVs were validated against tower observations at 8.5 m during a 40 second hovering period, resulting in an offset of 0.0 K to -0.7 K (not shown). Considering the sensor accuracy of $\pm$0.3 K and potential uncertainties due to spatial heterogeneity and disturbances from the airflow of seven drones hovering close together, we conclude that these errors are acceptable and smaller than the expected model bias. The fixed-wing UAVs for the soundings used hardware and software from the Paparazzi UAV open-source project (Hattenberger et al., 2014). Each sounding, as described by Groos et al. (2025), involved the UAV automatically following a predefined flight plan to measure vertical air temperature and humidity profiles. All measurements combined provide a comprehensive dataset for analyzing valley wind dynamics, atmospheric stratification, and glacier–valley exchange processes at high temporal and spatial resolutions.

https://doi.org/10.5194/egusphere-2026-3922
Preprint. Discussion started: 21 July 2026
© Author(s) 2026. CC BY 4.0 License.

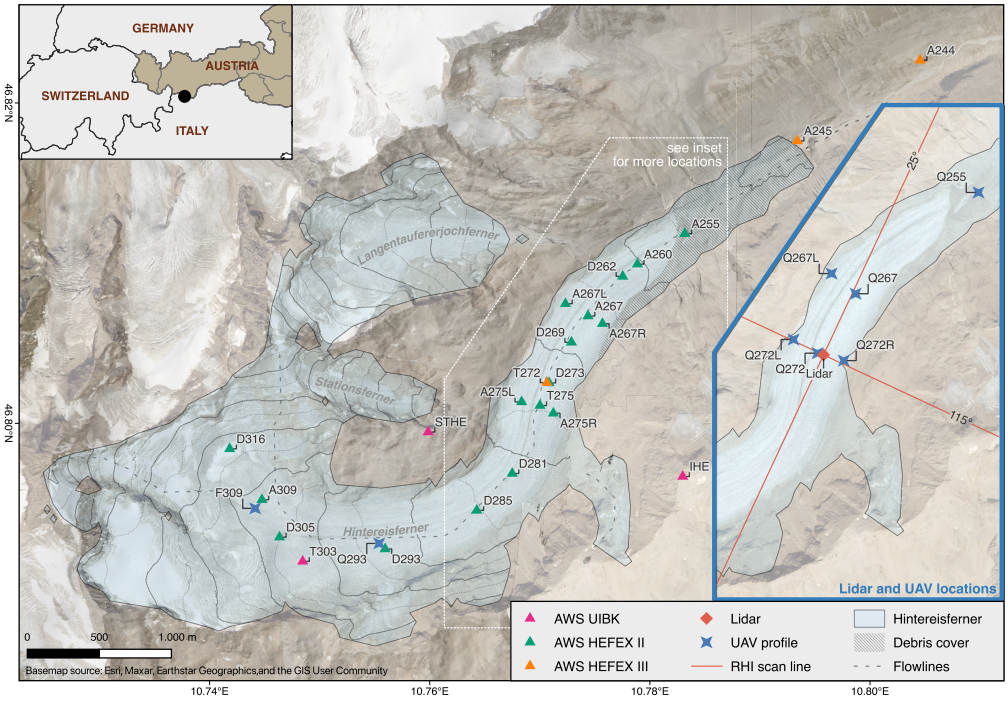

Figure 1. Map of study area and instruments, including the Hintereisferner glacier outline used in the ICON simulation. The locations of the observational platforms are indicated, including the AWSs installed during both field campaigns (green and orange triangles; station names include the site elevation divided by ten; the first letter represents station instrumentation as in Nicholson et al. (2025); the last letter L or R stands for left or right relative to the glacier flowline). The positions of UAV-based vertical profile measurements (blue stars) and ground-based lidar systems (red diamond) are marked together with the orientation of the RHI scanning transects (red line). Only measurement sites whose data are used in this study are included. The debris-covered part of the glacier was mapped by manually overlaying satellite imagery.

2.2 Overview of selected study periods

The analysis focused on two field campaigns, HEFEX II and HEFEX III, which together captured a broad range of synoptic forcing conditions and local atmospheric responses. During HEFEX II, the first half of the campaign was characterized by predominantly clear sky conditions with weak synoptic forcing. This was followed by the passage of a low-pressure frontal system that produced a severe storm, resulting in heavy rain and snowfall. Post-storm, temperatures gradually reverted to previous levels under renewed clear-sky conditions (Fig. A1; Nicholson et al., 2025).

While HEFEX III also started under clear-sky conditions, it was subsequently influenced by two synoptic low-pressure systems associated with moisture advection from the southwest. The latter event led to snowfall and temperatures around the freezing point at the main tower location (Fig. A2).

https://doi.org/10.5194/egusphere-2026-3922
Preprint. Discussion started: 21 July 2026
© Author(s) 2026. CC BY 4.0 License.

For an in-depth evaluation of near-surface thermodynamic variability, daily mean 2 m air temperature and specific humidity from the full weather station network were used to characterize spatial gradients and temporal variability within the surface layer over the approximately three-week period of HEFEX II.

Additionally, three distinct wind regimes from HEFEX II were intentionally chosen for different time periods, during which consistent and nearly steady meteorological conditions were present. This was done to evaluate the model's ability to reproduce katabatic flows under different synoptic influences: (i) a multi-day period of undisturbed katabatic flow under weak synoptic forcing with winds aligned along the down-glacier axis, representing a locally driven regime; (ii) a storm-driven episode with strong synoptic forcing and up-glacier flow, testing the model response when large-scale pressure gradients dominate local thermally driven circulations; and (iii) a transitional regime in which katabatic flow persists despite strong opposing easterly synoptic winds, providing a stringent test of flow superposition and competing forcings near the surface.

HEFEX III built upon the findings of HEFEX II, focusing on the structure and vertical evolution of the flow at the glacier-valley scale. A key event is the IOP from 7–10 August 2025, which includes coordinated UAV profiling every three hours under predominantly clear-sky conditions. This period is characterized by a pronounced diurnal cycle driven by strong radiative forcing, enabling the evaluation of the model's ability to capture the temporal evolution of temperature, stability, and vertical stratification up to 400 m AGL.

As a complementary case study, 10 August 2025 is selected for a full-day evaluation of the simulated flow evolution using continuous observations from both Doppler lidar systems. Throughout the day, the observations reveal pronounced variability in the local wind field, with several distinct flow patterns and transition periods driven by the interaction of glacier winds, topographic effects, and larger-scale atmospheric flow. The occurrence of multiple contrasting flow conditions within a single diurnal cycle makes this day particularly well suited for assessing the ability of ICON-LES to reproduce the highly variable and rapidly evolving flow regimes that characterize complex terrain. Continuous wind profiles within the lowest 200 m above the glacier surface are derived from the WindRanger lidar using the Velocity Azimuth Display (VAD) retrieval method, while additional RHI scans from the StreamLine lidar extend the analysis by capturing the spatial flow structure along both along-valley and cross-valley transects.

Together, the selected periods from both campaigns span a diverse set of synoptic conditions and dynamically distinct flow regimes at both the surface and valley scales, providing a comprehensive and process-oriented framework for evaluating the model against multi-platform observational datasets.

2.3 Model setup

ICON-LES is ideally suited for atmospheric modeling in complex terrain because of its nonhydrostatic dynamical core, unstructured triangular grid, and terrain-following vertical coordinates, which allow for an accurate representation of steep topography without introducing excessive numerical diffusion (Zängl et al., 2015). The LES configuration of the model explicitly resolves a wide range of turbulent eddies, thereby reducing the reliance on parameterizations that often struggle in heterogeneous mountain environments (Dipankar et al., 2015; Heinze et al., 2017). Its flexible grid refinement enables locally enhanced resolution over ridges, valleys, and slopes, effectively capturing terrain-induced flows, such as channeling, gravity wave gener-

https://doi.org/10.5194/egusphere-2026-3922
Preprint. Discussion started: 21 July 2026
© Author(s) 2026. CC BY 4.0 License.

Table 1. Overview of the defined model domains used for ICON-LAM. All domains use 46.80° N, 10.77° E as the center point.

Domain[a]	Half width lat, lon	Resolution	Area	Grid cells	Model levels	Min. layer thickness	Turbulent transfer	Time step
DOM02	1.50°, 2.00°	1 644 m	99 831 km^2	35 680	90	20 m	TURBDIFF[b]	5.0 s
DOM04	0.35°, 0.50°	411 m	6 114 km^2	34 964	90	20 m	3D Smagorinsky[c]	2.0 s
DOM06	0.10°, 0.15°	103 m	522 km^2	47 776	90	20 m	3D Smagorinsky[c]	1.0 s
DOM07	0.07°, 0.10°	51 m	242 km^2	88 640	150	10 m	3D Smagorinsky[c]	0.25 s

[a] The domains DOM01, DOM03, and DOM05 were skipped, [b] Raschendorfer (2001), [c] Smagorinsky (1963)

ation, and thermally driven circulations. Together, these features make ICON-LES a robust framework for studying boundary layer processes and turbulence in mountainous regions.

The model setup is based on ICON version 2024.10 and operates in the limited-area mode (ICON-LAM), utilizing a one-way nested configuration to achieve a target evaluation resolution of $\mathcal{O}(51\,\mathrm{m})$. The ICON-EU regional grid (R03B08), with a resolution of 6.5 km, served as the starting point for the domain definition. Four domains were defined (Zängl et al., 2022), each sharing the same central coordinates but with decreasing spatial extents (Table 1). To approach the finest grid spacing, the nominal resolutions of the domains were 1 644 m, 411 m, 103 m, and 51 m, where *resolution* is defined as the square root of the mean area of the triangular cells. Although ICON typically follows a factor-of-two refinement between domains, intermediate nests at coarser resolutions were omitted to reduce the computational cost. This configuration ensures that the innermost domain has sufficient grid points to capture the small-scale atmospheric processes relevant for model evaluation while maintaining feasible computational demands (Wagner et al., 2014).

All simulations in this study employed consistent model parameter settings across the respective domains to ensure comparability. The model time step was adjusted with increasing resolution, reaching 0.25 s for the highest-resolution domain. For the three innermost domains, large-eddy simulations were performed using the Smagorinsky diffusion scheme (Smagorinsky, 1963) with the stability correction of Lilly (1962), validated by Dipankar et al. (2015). Additionally, the number of iterations in the topography smoother was increased from one to two to enhance numerical stability by reducing small-scale orographic variability and associated pressure-gradient errors over steep terrain. For the finest domain, DOM07, the root-mean-square (RMS) height difference between neighboring grid points was reduced from 500 m to 100 m, further improving the fidelity of the terrain representation. All simulations used the Rapid Radiative Transfer Model (RRTM; Mlawer et al., 1997) as the radiation scheme.

The land surface representation in all simulations was provided by the ICON TERRA soil–vegetation–atmosphere transfer (SVAT) model (Heise et al., 2006; Schulz et al., 2016; Schulz and Vogel, 2020), which was chosen for its effectiveness in studies focused on surface fluxes of heat, moisture, and energy rather than long-term biogeochemical processes. TERRA requires a suite of external parameter fields, which were generated individually for each domain using ICON's default preprocessing data sources, supplemented with targeted manual updates to enhance local realism. Topography was derived from the ASTER digital elevation model (DEM; ASTER Science Team, 2019), and soil types were obtained from the FAO Digital Soil Map.

https://doi.org/10.5194/egusphere-2026-3922
Preprint. Discussion started: 21 July 2026
© Author(s) 2026. CC BY 4.0 License.

The monthly surface albedo fields were modified using MODIS satellite imagery (Schaaf and Wang, 2021) from the field campaign period to more accurately reflect the actual surface conditions. Land use classification was based on the GlobCover 2009 dataset (Arino et al., 2012), except for categories representing permanent snow and ice. In this class, glacier outlines were replaced with updated geometries from Open Global Glacier Model (OGGM; Maussion et al., 2019) simulations for the entire Alps. The default outlines were outdated and affected by interpolation errors that overestimated the glacier extent in the study area. Grid cells identified as ice-free in the OGGM data were reclassified into bare ground. OGGM simulations were performed under the SSP370 scenario using bias-corrected CMIP6 climate input from the ISIMIP3b framework based on the model MPI-ESM1-2-HR (Lange, 2019; Gutjahr et al., 2019).

The initial conditions and hourly lateral boundary conditions were obtained from the Pamore database (Deutscher Wetterdienst, 2026) of the German Weather Service (DWD), which provides operational access to ICON-based atmospheric fields. The outermost domain was forced with ICON-EU forecast data (6.5 km), and each successively finer domain used the output of its parent domain for boundary forcing. To ensure consistency with the modified land use representation, the initial conditions were adjusted for all grid cells reclassified as ice by assigning characteristic surface properties, such as appropriate density and temperature values. The simulations incorporated a spin-up period of one day, allowing the model state to dynamically adjust before the actual evaluation period.

The model output was recorded hourly, with additional wind fields averaged over 30 min to provide a more representative estimate of the mean atmospheric flow. The vertical grid structure resulted in the lowest model layer having a thickness of 10 m, providing output for prognostic variables at approximately 5 m AGL (lowest full-level center). Furthermore, the model output included diagnostic near-surface variables, such as temperature and humidity at 2 m.

2.4 Mapping observations to model grid

The model results were compared with observations using the grid cell containing the AWS location without applying spatial interpolation or averaging. Given the 51 m grid spacing, the AWS can be assumed to represent the conditions within that cell. Using direct grid cell values also avoids incorporating information from neighboring cells that may differ substantially in surface characteristics, such as elevation near steep mountain walls. Therefore, interpolation could introduce artificial smoothing and reduce the physical consistency of the comparison.

To compare with the UAV observations, the ICON grid column matching the UAV flight location was extracted for analysis. Given that UAV measurements have a significantly higher vertical resolution of approximately 1 m, the observations were mapped to the corresponding ICON model layers. All measurement points falling within the vertical extent of a model layer were averaged and compared with the model values at the respective full-level centers. This approach ensured a consistent comparison between the high-resolution observations and model representation.

Different approaches were applied for a comparison with Doppler lidar observations depending on the scan geometry. For the WindRanger 10° PPI scan, the ICON grid column containing the lidar location was identified, and the corresponding model values were directly compared with lidar measurements. For the StreamLine RHI scan, which measures the radial velocity, a vertical plane representing the RHI scan line was constructed and intersected with the ICON grid. The simulated

https://doi.org/10.5194/egusphere-2026-3922
Preprint. Discussion started: 21 July 2026
© Author(s) 2026. CC BY 4.0 License.

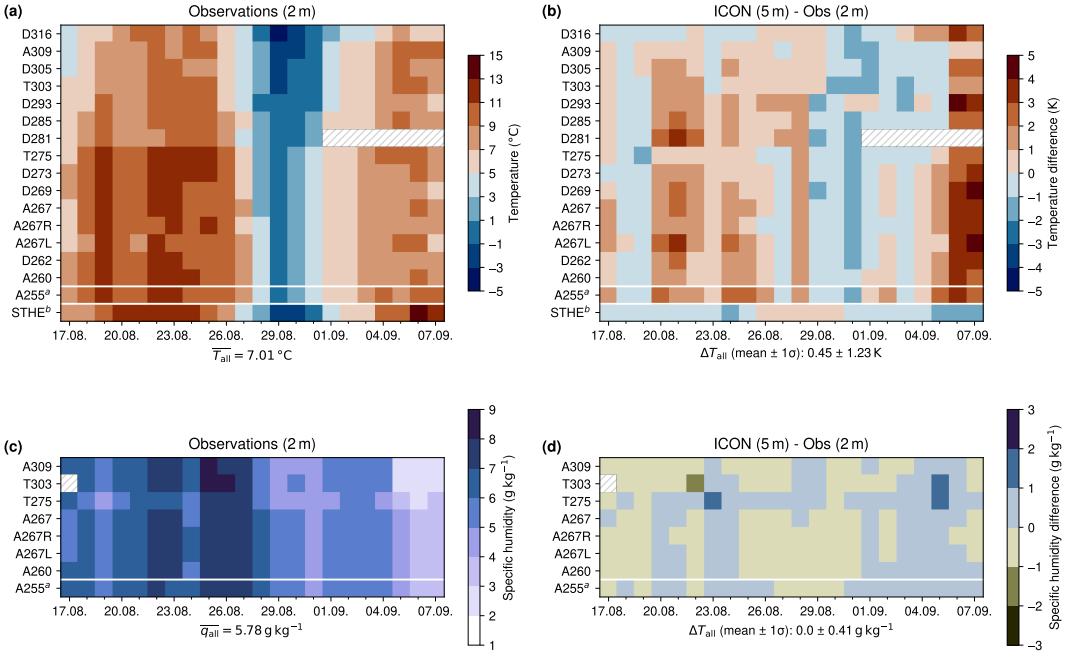

Figure 2. Spatial distribution of near-surface measurements and model deviations for the HEFEX II station network. Panels **(a)** and **(c)** show the observed daily mean air temperature and specific humidity at 2 m AGL. Panels **(b)** and **(d)** show the corresponding differences between ICON-LES and observations, computed from model output at 5 m height. Hatching indicates missing measurements. Note that station A255^a is located on debris-covered ice, and station STHE^b is located off-glacier.

wind components (u, v, and w) were interpolated onto this plane and projected onto the lidar line of sight originating from the instrument location, allowing the corresponding model-derived radial velocity to be calculated and compared with the observations.

3 Results and discussion

3.1 Representation of near-surface meteorological variables

The comparison of daily mean near-surface air temperature and specific humidity between the ICON-LES simulations and the observational dataset demonstrates that the model is generally capable of reproducing the observed spatial and temporal variability across all stations and both campaigns (Fig. 2 and A4). In particular, the spatial patterns are accurately captured under varying synoptic conditions, indicating that mesoscale flow structures and terrain-induced circulations are realistically represented, and that ICON effectively simulates large-scale advection.

https://doi.org/10.5194/egusphere-2026-3922
Preprint. Discussion started: 21 July 2026
© Author(s) 2026. CC BY 4.0 License.

3.1.1 Air temperature from AWS

The analysis further revealed that ICON's prognostic 5 m temperatures provide substantially better agreement with observations than the diagnostic 2 m outputs, especially at on-glacier stations (Fig. 2b and A3b). Over melting ice and under thermally stable boundary layer conditions, strong temperature gradients can develop within the lowest few meters of the atmosphere. These gradients suppress turbulent mixing, thereby reducing the exchange of heat, moisture, and momentum between the ice surface and overlying air (Mahrt, 2014). Consequently, the near-surface atmosphere can become partially decoupled from the ice surface (Bugnard et al., 2025). Under such conditions, the assumption of the underlying Monin–Obukhov similarity theory (MOST) of fully developed turbulence is violated, resulting in known performance limitations (e.g., Sauter et al., 2026; Casasanta et al., 2025; Maronga et al., 2020). Thus, ICON's diagnosed 2 m temperature tends to overestimate surface cooling over ice, producing unrealistically low near-surface temperatures. To overcome this limitation, we compared the observations with the prognostic temperature at 5 m.

Near-surface observations from HEFEX II show an elevation-dependent temperature change, with stations located up to 2 750 m showing higher temperatures than those above 2 800 m ASL. ICON effectively captures this gradient but exhibits a small systematic overall warm bias ($\pm 1\sigma$) of +0.45 $\pm$ 1.23 K during HEFEX II (Fig. 2b) and a slight overall cold bias of -0.28 $\pm$ 0.95 K during HEFEX III (Fig. A4b). The discrepancies between the model output and observations at stations with similar surface characteristics arise mainly from temporal differences rather than spatial variations.

A pronounced warm bias was identified at on-glacier stations, particularly during clear-sky conditions between 20–22 August and again after 5 September 2023. Under these conditions, a deeper katabatic layer and surface inversion form, embedding the 2 m observation level and leading to colder temperatures. In contrast, the 5 m temperature in ICON is less directly affected by these near-surface gradients, contributing to the simulated warm bias relative to the observations. In general, comparing the 5 m ICON temperature with 2 m observations remains reasonable because the katabatic jet maximum and surface inversion at HEF are typically observed below 2 m (Mott et al., 2020, 2025; Nicholson et al., 2025) and temperature stratification is often substantially weaker above this layer. Evidence for these extremely sharp near-surface gradients is provided by the observational comparison between 2 m and 4 m measurements (Fig. A1), which reveal temperature differences of up to 5 K. Comparable magnitudes have been reported in previous glacier boundary layer studies, where vertical temperature differences of up to 15 K within the lowest 4 m were observed over glacier surfaces during katabatic flow conditions (Oerlemans and Grisogono, 2002).

When the evaluation was restricted to the on-glacier stations T275 and T303, where continuous observations at both 2 m and 4 m were available, the comparison revealed a clear dependence of the model bias on the observation height (Table 2). Compared against the 2 m measurements, the simulations shows a bias of +0.02 $\pm$ 1.48 K, whereas comparison against the 4 m observations result in a slight cold bias of -0.34 $\pm$ 1.05 K. This further supports the interpretation that the apparent overall warm bias is primarily linked to unresolved shallow inversions in the lowest meters above the glacier surface, rather than a systematic overestimation of atmospheric temperature by the model itself.

https://doi.org/10.5194/egusphere-2026-3922
Preprint. Discussion started: 21 July 2026
© Author(s) 2026. CC BY 4.0 License.

Table 2. Statistical summary of model deviations for near-surface variables during HEFEX II and HEFEX III campaigns. For each campaign, results are separated by surface type (on-glacier and off-glacier) and measurement height (2 m and 4–5 m, where available). Reported metrics include the mean bias and one standard deviation ($\pm 1\sigma$) for air temperature (ΔT) and specific humidity (Δq), calculated from variables aggregated to 3 hour mean values. In addition, the mean elevation difference ($\overline{\Delta z}$) between the model topography and the actual station elevation is provided to quantify terrain representation errors.

	HEFEX II				HEFEX III		
	on-glacier (all)	on-glacier (T275 and T303)		off-glacier (all)	on-glacier (all)		off-glacier (all)
	2 m	2 m	4-5 m	2 m	2 m	4-5 m	2 m
# of paired obs.* (N)	2528 / 1186	344 / 329	329	172 / 0	411 / 405	411 / 197	510
$\overline{\Delta z}$ in m	61.35	45.17	45.17	7.57	49.86	49.86	-1.89
ΔT (mean $\pm$ 1σ) in K	0.42 $\pm$ 1.65	0.02 $\pm$ 1.48	-0.34 $\pm$ 1.05	-0.47 $\pm$ 0.99	0.12 $\pm$ 1.24	-0.39 $\pm$ 1.06	-0.23 $\pm$ 1.26
Δq (mean $\pm$ 1σ) in g kg^{-1}	0.01 $\pm$ 0.87	0.16 $\pm$ 0.92	-0.73 $\pm$ 1.77	NA	-0.02 $\pm$ 0.89	0.07 $\pm$ 0.86	-0.22 $\pm$ 0.97

* Different numbers for temperature / humidity observations due to station equipment.

Given the sensitivity of the results to measurement height and stratification regime, the findings demonstrate the need for increased vertical resolution within the lowest tens of meters to adequately resolve shallow katabatic flow and the associated stable boundary layer processes over glacierized terrain. In particular, the current lowest full-level center, at approximately 5 m AGL, appears to be insufficient to resolve the observed very shallow surface inversions. Observational studies at HEF and other valley glaciers in the Alps have shown that the katabatic low-level jet often occurs at heights around 2 m above the surface (e.g., Nicholson et al., 2025; Mott et al., 2025, 2020; Oerlemans and Grisogono, 2002). Resolving such small-scale flow features demands substantially finer vertical discretization near the surface, requiring horizontal resolutions of about 5 m (Cuxart, 2015), which remains computationally too expensive for the current configuration and domain size.

During periods of neutral stratification and well-mixed conditions, when there was no significant temperature difference between the 2 m and 4 m observations (Fig. A1), such as during the storm event between 29–31 August 2023, the simulations showed a slight cold bias at the on-glacier stations. Under these circumstances, the remaining deviations are more likely related to differences in elevation (Δz; Table 2) between the model and the actual stations than to boundary layer processes. The glacier surface elevation in ICON is generally higher than the elevation of the AWS locations because an outdated DEM was used, which does not fully account for recent glacier thinning. This discrepancy can be as much as 100 m in the lower part of the glacier. Consequently, simulated temperatures are expected to be lower due to the adiabatic lapse rate, which provides a plausible explanation for the observed cold bias during well-mixed conditions.

A clear dependence on the surface type is also evident. In contrast to the on-glacier locations, ICON slightly underestimates air temperatures at stations in the glacier forefield (stations A244 and A245; Fig. A4) and the more exposed off-glacier stations, STHE and IHE, which exhibit substantially larger temperature fluctuations than the on-glacier and forefield stations. This behavior reflects a stronger coupling to atmospheric forcing and reduced surface damping. ICON reproduces these enhanced

https://doi.org/10.5194/egusphere-2026-3922
Preprint. Discussion started: 21 July 2026
© Author(s) 2026. CC BY 4.0 License.

variations particularly well at STHE and IHE, resulting in negligible mean deviations at these locations of -0.23 $\pm$ 1.26 K (HEFEX III in Table 2), despite the larger amplitude of observed temperature variability. The off-glacier stations also show high agreement with the diagnostic 2 m temperature output indicating an effective land surface parameterization (Fig. A5).

3.1.2 Specific humidity from AWS

The ICON simulations generally reproduce the evolution of near-surface specific humidity well throughout both campaigns (Fig. 2d and A4d). For HEFEX II, the overall mean bias is 0 $\pm$ 0.41 g kg^{-1}, indicating an excellent representation of near-surface humidity throughout the campaign, including a distinctly wetter period around 26 August and a very dry period from 5 September 2023. This strong agreement suggests that near-surface moisture variability is primarily governed by advection, large-scale mixing, and phase change processes, all of which are well represented in the model. Turbulent moisture exchange also appears to be less sensitive to near-surface stability than sensible heat flux, the latter of which depends strongly on temperature gradients and associated stability corrections (Conway and Cullen, 2013).

In contrast, during HEFEX III, ICON shows an overall slight dry bias of -0.19 $\pm$ 0.69 g kg^{-1}. This bias can be mainly attributed to two specific days, 14 and 19 August 2025 (Fig. A4), and more pronounced at off-glacier stations (Table 2). On these days, the model systematically underestimates the specific humidity at all stations. These deviations are best interpreted as timing errors, rather than systematic biases. On both days, the model responds to the moistening of dry conditions with a delay, a behavior commonly reported in NWP simulations over complex terrain (Sauter et al., 2026). This time lag likely reflects an overly persistent stable stratification, which inhibits the downward mixing of moist air or delays the transition to a less stable regime. Outside these periods, the simulated humidity aligns with the observed temporal evolution.

Overall, ICON accurately reflects the magnitude of specific humidity and its temporal variability, regardless of whether conditions are moist or dry and regardless of station location, including on-glacier, off-glacier, and glacier forefield sites. These results indicate that the main deficiencies in the model are limited to event-specific, near-surface thermodynamic processes over glacier ice, such as entrainment from aloft, rather than errors in large-scale moisture transport or sensitivity to synoptic forcing.

3.1.3 Flow patterns under different synoptic conditions

The period from 20–25 August 2023 was characterized by a stable synoptic regime with fair-weather conditions and warm air masses over the glacier, favoring thermally stable stratification. Synoptic forcing was weak throughout this period, as indicated by 500 hPa wind speeds generally below 10 m s^{-1} (Fig. 3a). Observations show a well-developed and undisturbed katabatic flow along the flowline at all AWS locations, with wind speeds measured at 2–3 m AGL typically around 4 m s^{-1} and increasing toward the lower glacier.

Overall, ICON reproduces both the katabatic flow and near-surface temperature reasonably well, although it underestimates wind speeds by approximately 1–2 m s^{-1} and retains the small warm bias discussed earlier. The wind speed is expected to be underestimated, as the katabatic jet maximum at HEF is often observed at heights of only 1–2 m AGL (e.g., Nicholson et al., 2025; Mott et al., 2025), which is below the lowest model level. Interestingly, WRF simulations performed in the same region

https://doi.org/10.5194/egusphere-2026-3922
Preprint. Discussion started: 21 July 2026
© Author(s) 2026. CC BY 4.0 License.

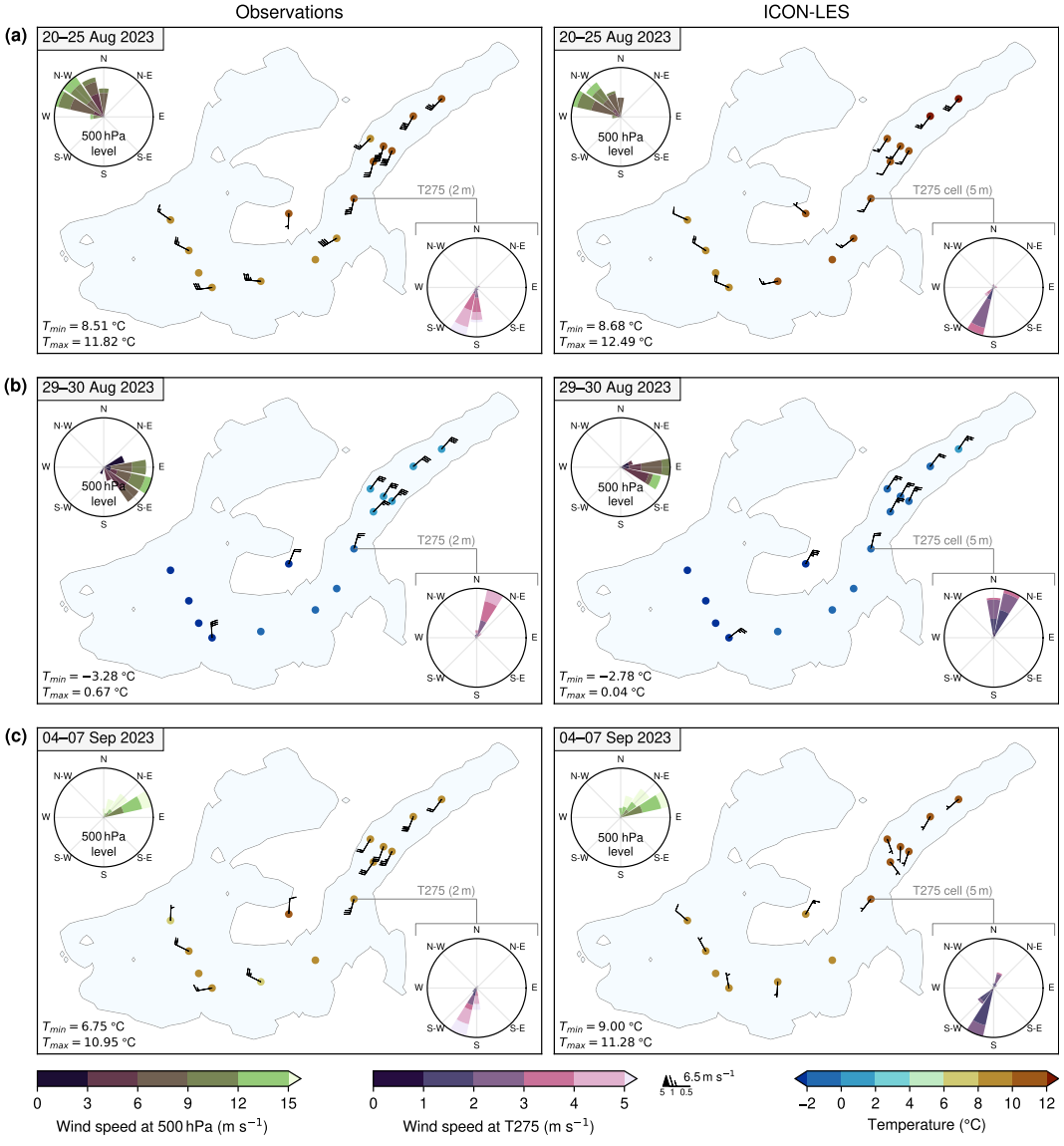

Figure 3. Panels represent three distinct flow regimes during HEFEX II, characterized by **(a)** undisturbed katabatic flow, **(b)** up-glacier flow during a storm event, and **(c)** katabatic conditions under opposing synoptic forcing. Observed and simulated mean wind speed and direction for all stations with sufficient data during each period are shown as wind barbs. Wind roses show near-surface winds at the tower site T275 in purple and winds at 500 hPa in green. Upper-level observations are derived from hourly ERA5 reanalysis data (Hersbach et al., 2023). Scatter points indicate the corresponding mean temperature for each selected period.

at comparable horizontal resolution tend to overestimate near-surface wind speeds, even though the lowest model output is slightly higher at 7 m AGL (Goger et al., 2022).

https://doi.org/10.5194/egusphere-2026-3922
Preprint. Discussion started: 21 July 2026
© Author(s) 2026. CC BY 4.0 License.

The spatial distribution of maximum wind speeds also differs between observations and simulations. While the observations indicate local wind maxima downstream of station T275, ICON places the strongest winds at the location closest to the glacier terminus. A plausible explanation for this discrepancy is the model representation of surface properties in the lower glacier region. In reality, the glacier tongue is entirely debris-covered (Fig. 1), resulting in modified surface roughness characteristics, surface energy exchanges, and boundary layer development (Collier et al., 2015). However, ICON does not explicitly account for debris-covered ice surfaces because of the absence of a dedicated land cover class.

In contrast, during the storm event, characterized by strong easterly synoptic forcing and a well-mixed, nearly neutrally stratified boundary layer, the local katabatic wind system is eroded (Fig. 3b). This results in up-valley flow across the glacier, as observed and simulated at all AWS locations with available data. Data availability, especially at higher elevations, was limited due to power outages and storm-related instrument failures. ICON more accurately reproduces wind speeds during this event than during the other investigated periods.

This behavior is consistent with previous studies showing that the influence of land surface processes diminishes when large-scale atmospheric forcing dominates (Haualand et al., 2025). The improved model performance under storm conditions suggests that momentum transport is more realistically represented when mechanically generated turbulence prevails over buoyancy-driven processes.

As previously discussed, ICON tends to underestimate temperatures under well-mixed conditions. The simulated temperature fields exhibit the strongest cold bias at lower elevations, where the difference in elevation between the model and the actual terrain is greatest. At the same time, minimum temperatures are overestimated, indicating insufficient nocturnal cooling or excessive vertical mixing within the near-surface layer during storm conditions.

In conditions where the katabatic flow remains established despite opposing east-northeasterly synoptic forcing (Fig. 3c), ICON produces very low wind speeds across the glacier, whereas observations at 2 m continue to indicate a well-developed katabatic circulation with magnitudes comparable to those observed under undisturbed conditions (Fig. 3a). This demonstrates the persistence of thermally driven downslope flow, even when conflicting large-scale forcing is present. The simulated wind field also exhibits greater directional variability, likely due to the generally weak modeled wind speeds. This is consistent with previous studies showing that wind direction becomes increasingly uncertain and less meaningful under low-wind conditions (He et al., 2023).

The inability of ICON to sustain the observed katabatic flow suggests that the model overestimates the influence of the opposing synoptic flow and fails to adequately represent the shallow density-driven flow near the glacier surface. Several factors may contribute to this behavior, including excessive turbulent mixing, insufficient vertical resolution within the lowest meters above the surface, underestimation of the strong near-surface static stability, and inadequate representation of shallow slope-parallel momentum transport that supports katabatic acceleration (Goger et al., 2022). These findings again confirm that the model resolution is insufficient to capture smaller-scale boundary layer features, such as the shallow katabatic jet (Cuxart, 2015). Consistent with this interpretation, this period exhibits the largest warm bias in the simulated 2 m air temperature among all investigated regimes. This temperature bias is consistent with the presence of a shallow near-surface inversion layer below the lowest model level, as previously discussed. Since the model cannot fully resolve the inversion, near-surface temperatures

https://doi.org/10.5194/egusphere-2026-3922
Preprint. Discussion started: 21 July 2026
© Author(s) 2026. CC BY 4.0 License.

Table 3. Statistical evaluation of vertical potential temperature profiles obtained from all UAV soundings conducted during both IOPs of HEFEX III. Reported statistics quantify the overall model performance in reproducing the observed thermodynamic stratification within the lower atmosphere above the glacier.

	IOP1							IOP2		
	Q255	Q267	Q267L	Q272	Q272L	Q272R	F309	Q257	Q272	Q293
# of paired obs.* (N)	499	314	211	565	184	222	463	219	220	255
coefficient of determination (R^2)	0.83	0.69	0.72	0.83	0.68	0.81	0.74	0.88	0.91	0.86
mean absolute error (MAE)	0.81	0.88	0.87	0.82	0.96	0.92	0.89	0.55	0.56	0.48
mean bias error (MBE)	-0.22	-0.17	-0.15	-0.32	-0.10	-0.40	-0.54	0.05	-0.36	-0.13
root mean square error (RMSE)	1.12	1.10	1.08	1.12	1.26	1.11	1.11	0.71	0.75	0.62

* Deviations in the number of paired observations during IOP1 arise from differences in maximum profile height, with soundings at Q255 and Q272 reaching 400 m AGL, while profiles at other locations were limited to 200 m. During IOP2, all UAV soundings reached 400 m, but the total number of flights was lower due to the shorter observation period.

become overly warm. This reduces the density contrast between air masses near the surface and the overlying atmosphere, consequently weakening the thermally driven forcing of the katabatic flow.

Together, these findings suggest that the model's representation of the shallow stable boundary layer, rather than deficiencies in the large-scale flow field, is the primary source of error in this regime. This behavior contrasts with runaway cooling reported in models that excessively dampen turbulent fluxes (Conway and Cullen, 2013). In those models, overly suppressed mixing leads to exaggerated near-surface cooling and overly strong stability. In the present case, however, the bias structure is more consistent with insufficient decoupling and excessive mixing, which weakens near-surface stratification rather than amplifying it (Bugnard et al., 2025).

3.2 Representation of valley atmosphere stratification and flow

3.2.1 Potential temperatures from UAV soundings

UAV observations provide a detailed view of vertical stratification that cannot be resolved by surface measurements alone (Groos et al., 2025). Figure 4 illustrates the observed and simulated potential temperature profiles at the tower location (Q272) derived from quadcopter measurements taken up to 400 m AGL during the first IOP of HEFEX III from 6–10 August 2025. The observations show a distinctly colder phase at the beginning of the IOP, followed by an increase in potential temperatures from 8 August onward, particularly during the afternoon hours. ICON reproduces this overall temporal evolution well and captures the diurnal cycle of daytime warming and nighttime cooling. The model also shows a strong agreement with the observed temporal and vertical variability, reflected by a coefficient of determination (R^2) value of 0.83 at location Q272 (Table 3).

Despite the generally good agreement, several deviations indicate errors in the timing of the boundary layer transition processes. A comparison of vertical soundings on 8 August reveals that ICON is too cold throughout the entire profile at

https://doi.org/10.5194/egusphere-2026-3922
Preprint. Discussion started: 21 July 2026
© Author(s) 2026. CC BY 4.0 License.

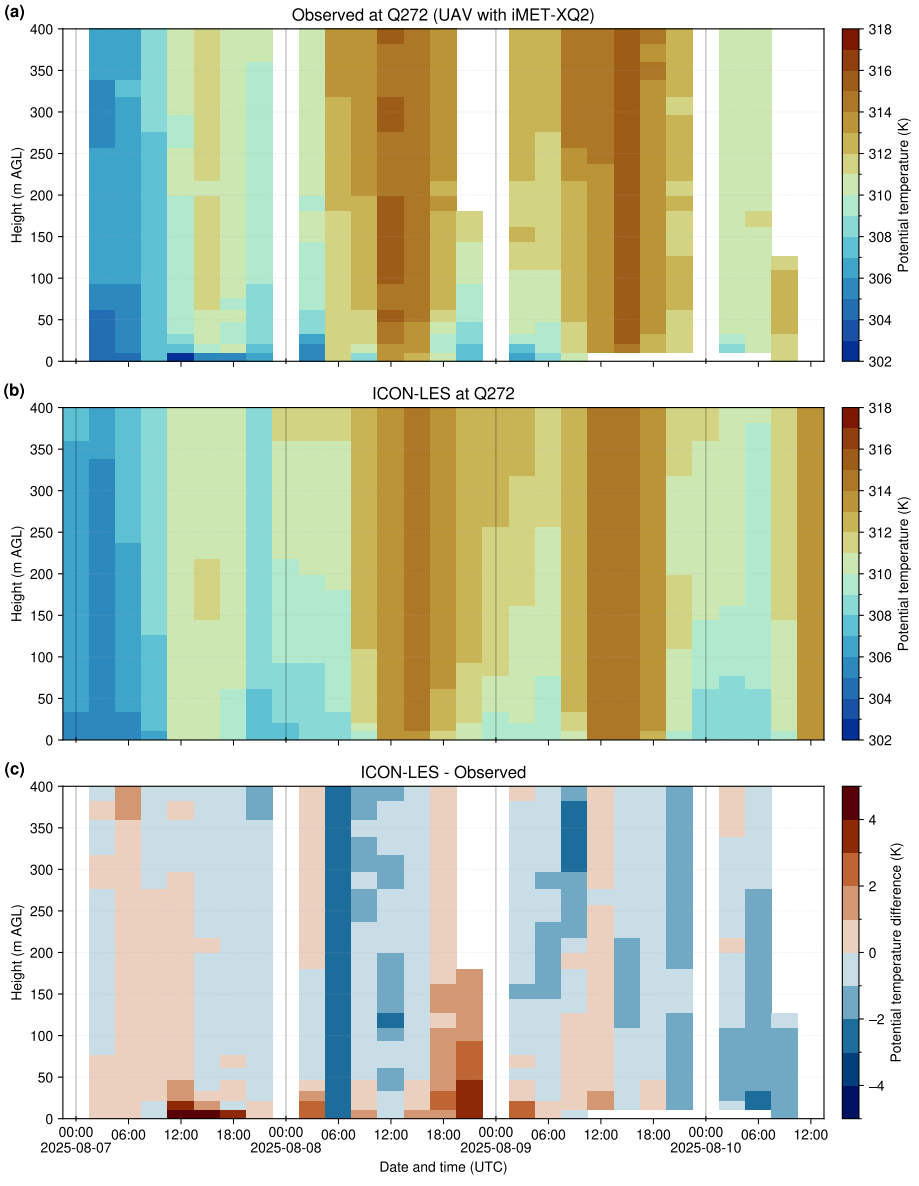

Figure 4. Vertical profiles of potential temperature up to 400 m AGL at location Q272 during the first IOP of HEFEX III (7–10 August 2025). Panel **(a)** shows the observed profiles, panel **(b)** presents the corresponding ICON model output, and panel **(c)** depicts the difference between both.

06 UTC, while it remains too warm during the evening hours (18 and 21 UTC), with the largest deviations occurring near the surface. During the intermediate period, the deviations are comparatively smaller, suggesting a better representation of the daytime evolution of the boundary layer. The sign reversal from a morning cold bias to an evening warm bias suggests a delayed transition from nocturnal stable conditions to daytime mixing, followed by delayed evening cooling and overly

https://doi.org/10.5194/egusphere-2026-3922
Preprint. Discussion started: 21 July 2026
© Author(s) 2026. CC BY 4.0 License.

persistent turbulent mixing. Similar morning cold biases are also present on 10 August, although they are confined to the lowest levels. In contrast, the adjacent days (7 and 9 August) do not exhibit comparable deviations, indicating that these timing errors are event-specific rather than persistent. Such behavior is consistent with commonly reported errors in the representation of boundary layer adjustment processes (Sauter et al., 2026). Overall, the UAV comparison shows a cold bias in ICON of -0.32 $\pm$ 1.07 K (Table 3), which is consistent with the near-surface AWS validation at 4 m (Table 2).

While some errors may be due to real model biases, others are likely related to imperfect UAV observations. The measurements themselves are subject to uncertainties associated with sensor response times in strong temperature gradients (Hansche et al., 2023), radiative effects (Kimball et al., 2020b), and limited ventilation during low-wind conditions. The iMet-XQ2 sensor has a stated accuracy of $\pm$0.3 K, placing the observed mean bias only marginally outside the instrumental uncertainty range. Furthermore, radiative influences may persist despite the use of radiation shields and adherence to established sensor deployment guidelines (e.g., Kimball et al., 2020a; Greene et al., 2019), particularly during periods of strong solar radiation and weak ventilation. Although these factors may contribute to minor temperature errors, the coherent structures observed in the profiles and their consistent reproduction by ICON support that UAV observations are suitable for model evaluation.

While the model exhibits an overall cold bias throughout much of the valley atmosphere, the lowest model level is predominantly warmer than observed, particularly during afternoon periods such as 7 August. This warm bias is confined to the lowest layer(s) and coincides with an underestimated katabatic jet (Sect. 3.1). It likely reflects excessive turbulent mixing and/or insufficient near-surface cooling in the model, which reduces the temperature gradient that drives katabatic acceleration over the glacier. In addition, the shallow surface-based inversion may not be fully resolved at 10 m vertical resolution, further contributing to overly warm near-surface conditions. Although a model-related origin is therefore likely, a potential cold bias in the UAV measurements near the ice surface cannot be entirely ruled out. During ascent from the ice surface, sensor inertia may cause the temperature sensor to respond too slowly to strong vertical temperature gradients, resulting in slightly underestimated temperatures at the bottom of the profile.

As shown in Table 3, all locations show a comparable cold bias, with good agreement between observations and simulations. The highest R^2 values occur for IOP2 and at Q255 and Q272, where flights reached 400 m AGL and therefore sampled a larger fraction of the valley atmosphere. In contrast, flights at other locations were limited to 200 m, increasing the relative influence of the lowest levels where both model and measurement uncertainties are largest. The improved agreement at higher flight altitudes therefore suggests that ICON represents the valley atmosphere more accurately than the near-surface layer, indicating that excessive warming in the model does not extend into the overlying valley atmosphere (Bugnard et al., 2025).

3.2.2 In-valley flow from Doppler lidar scans

A full-day case study conducted on 10 August 2025 provides a comprehensive evaluation of the simulated valley and glacier wind system under varying synoptic conditions. Throughout the day, the ERA5 reanalysis data indicate a gradual evolution of the large-scale flow (Fig. A2), while observations reveal distinct in-valley flow signatures, highlighting the complex interplay between synoptic forcing, glacier winds, and orographic influence. This succession of regimes is representative of the multi-scale complexity that characterizes mountain boundary layer dynamics in enclosed Alpine valleys (e.g., Serafin et al., 2018;

https://doi.org/10.5194/egusphere-2026-3922
Preprint. Discussion started: 21 July 2026
© Author(s) 2026. CC BY 4.0 License.

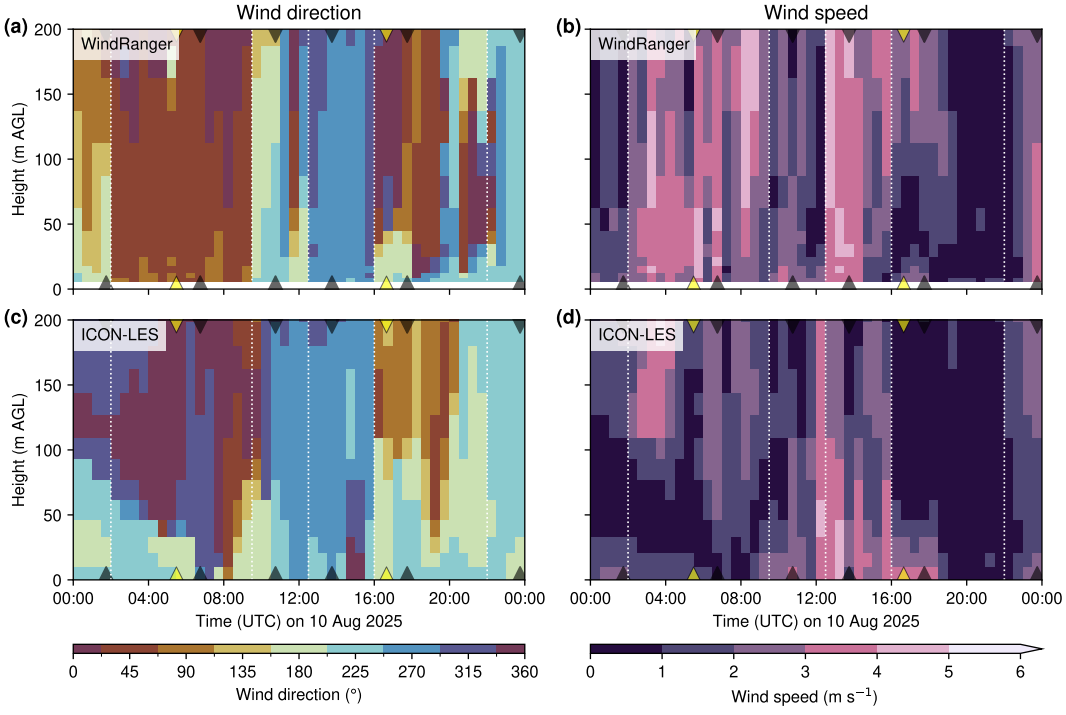

Figure 5. Diurnal evolution of wind direction and wind speed in the lowest 200 m AGL close to location T272 (HEFEX III tower site; red diamond in Fig. 6) on 10 August 2025, based on 30 min averages. Panels **(a)** and **(b)** show observations from the WindRanger Doppler lidar derived from PPI scans, representing wind direction and wind speed, respectively. Panels **(c)** and **(d)** show the corresponding variables from the ICON-LES simulation. White dotted lines indicate transitions between the identified flow patterns during the diurnal cycle. Yellow triangles mark sunrise and sunset times. Black triangles highlight selected time periods for which detailed RHI-based analyses are presented in Fig. 6.

Zardi and Whiteman, 2013), making this case particularly interesting and challenging to reproduce. WindRanger PPI scans (Fig. 5) provide 30 min averaged wind profiles of the lowest 200 m AGL. Spatial context is added by StreamLine RHI scans (Fig. 6) along the glacier flowline (25° azimuth) and across the glacier (115° azimuth) at selected time steps.

During the first part of the night (until 02:00 UTC; Fig. 5 and 6a), strong westerly synoptic forcing is present above the surrounding ridgelines, influencing the flow aloft. Both the observations and ICON represent weak down-glacier winds at the lowest 75-100 m AGL. The main discrepancy occurs above this layer. While ICON transitions to flow aligned with the prevailing northwesterly synoptic forcing, the observations reveal southeasterly to easterly winds (Fig. 5). This flow cannot be explained by large-scale forcing alone. Although the exact mechanism cannot be determined from the available observations, it is likely associated with a complex interplay within the glacier-valley system involving gravity waves, flow deflection, and other orographic effects acting in combination with the strong synoptic flow (Lehner and Rotach, 2018; Goger et al., 2022). Consequently, ICON captures the down-glacier winds but fails to reproduce the observed flow structure in the layer above.

https://doi.org/10.5194/egusphere-2026-3922
Preprint. Discussion started: 21 July 2026
© Author(s) 2026. CC BY 4.0 License.

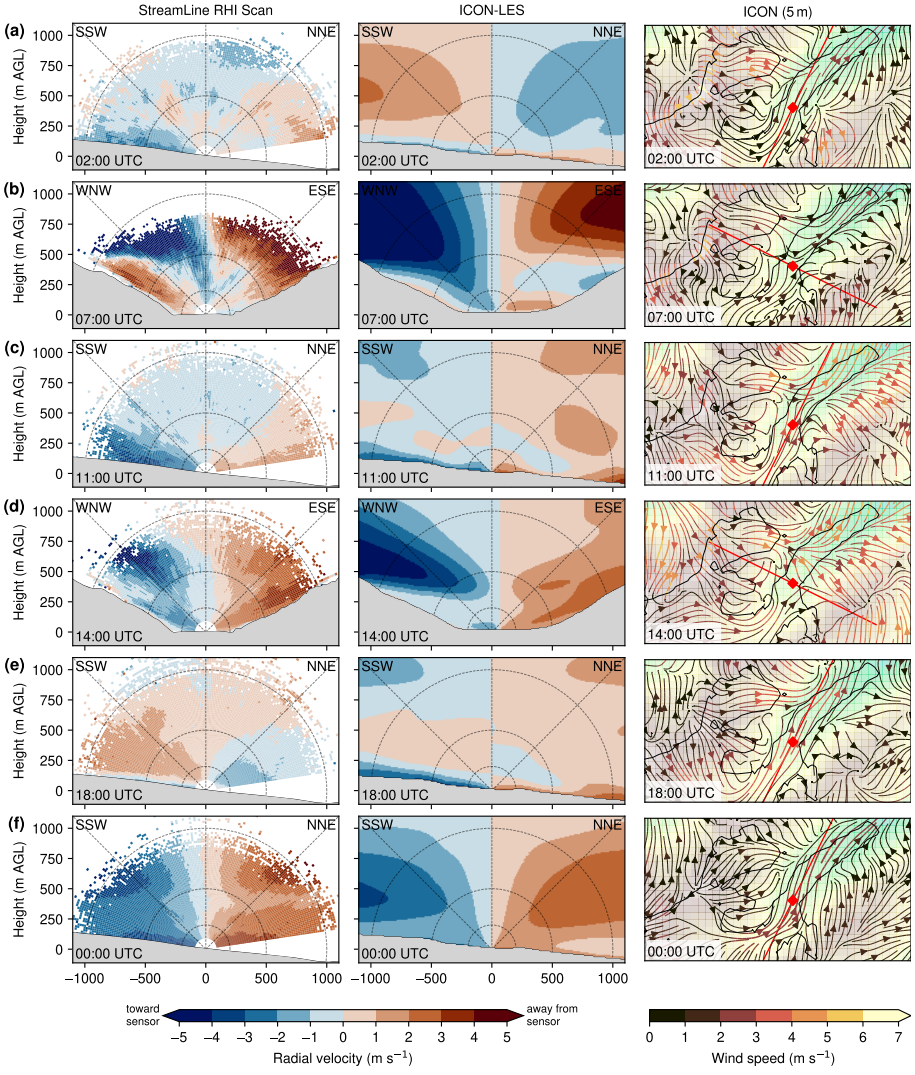

Figure 6. Comparison of observed and simulated radial velocity fields during the case study on 10 August 2025. Each row represents a 30 min averaged time period, illustrating the temporal evolution of the glacier-valley circulation throughout the day. The first column shows radial velocity measured by the StreamLine Doppler lidar from RHI scans performed either along the glacier flowline or across the valley. The second column shows the corresponding radial velocity derived from the ICON-LES simulation and interpolated onto the same scanning geometry. The third column shows the simulated near-surface horizontal wind field, including the respective lidar scan axis, added for reference. Positive and negative radial velocities indicate movements directed away from and toward the lidar, respectively. Time stamps denote the end of the averaging interval.

The period between 02:00 and 09:30 UTC reveals the largest disagreement between observations and model results. In contrast to the preceding phase, the previously observed down-glacier wind is fully eroded at the lidar location by pronounced easterly to northeasterly up-valley flow with wind speeds exceeding 5 $\mathrm{m\,s^{-1}}$, as seen in the WindRanger observations. Given

https://doi.org/10.5194/egusphere-2026-3922
Preprint. Discussion started: 21 July 2026
© Author(s) 2026. CC BY 4.0 License.

the persistent northwesterly synoptic forcing and the pre-sunrise timing, this flow cannot readily be explained by either synoptic forcing or the thermally driven valley circulation. Additionally, RHI scans reveal a pronounced upslope wind along the WNW valley sidewall, indicating a strong lateral flow asymmetry likely driven by terrain-induced effects. ICON, in contrast, retains a katabatic layer near the surface (cyan in Fig. 5), while the flow aloft remains broadly aligned with the northwesterly synoptic background and fails to reproduce both the observed up-valley regime (Fig. 5) and the pronounced sidewall flow structure (Fig. 6b). Compared with UAV-based measurements, ICON also exhibits a cold bias of up to -2 K within the lowest 100 m AGL (Fig. 4), which may contribute to excessive stability and the persistence of near-surface down-glacier wind. Accurate representation of the valley-scale temperature structure therefore remains crucial for correctly simulating the coupling between thermal forcing and orographically driven circulation (Schmidli and Quimbayo-Duarte, 2023). After approximately 08:00 UTC, both observations and model show a gradual transition toward up-valley flow (Fig. 5), indicating that ICON responds adequately to surface heating once insolation develops.

Between 09:30 and 12:30 UTC, synoptic forcing weakens and shifts toward northwesterly direction. Tower measurements indicate the development of a shallow daytime katabatic flow near the glacier surface (Fig. A2) that is not strongly affected by winds above. The down-glacier flow near the surface is reproduced by ICON, although not as deep (Fig. 6c). Furthermore, the simulation shows the westerly flow developing earlier and being more pronounced and vertically coherent than the observations (Fig. 5).

From 12:30 to 16:00 UTC, a topographically modified westerly flow dominates the entire observed profile and reaches the surface (Fig. 5) despite only weak large-scale forcing. RHI scans suggest a deep flow layer extending to approximately 500 m AGL (Fig. 6d). The direction, depth, and persistence of this flow align with those of a gap or channeled flow funneled through the topographic saddle that previously connected the Stationsferner and Langtaufererjochferner tributary glaciers to the Hintereisferner (Fig. 1). This local flow feature under westerly synoptic forcing is in line with previous studies by Mott et al. (2020) and Goger et al. (2022). Both observations and ICON capture this flow pattern remarkably well, reproducing the observed wind directions and magnitudes throughout most of the profile, with a slight underestimation of wind speeds in the upper levels (Fig. 5d). However, the transition into this flow regime and the decay of the near-surface flow appear smoother in the model than in the observations. This likely reflects differences in topography and the model's limited ability to resolve intermittent terrain-induced flow variability.

During the late afternoon and evening (16:00 to 22:30 UTC), the topographically induced westerly flow weakens. Simultaneously, both WindRanger and RHI observations indicate the redevelopment of the glacier wind. ICON reproduces the timing of the transition but overestimates the depth and intensity of the near-surface katabatic layer (Fig. 6e). The excessive layer thickness is evident in both lidar datasets and is consistent with the tendency of ICON to overestimate the depth of stable near-surface flow layers. In addition, the model overestimates near-surface wind speeds in the evening (Fig. 5d). This behavior is similar to the findings of Goger et al. (2022), whereas ICON and other models more commonly exhibit an underestimation of near-surface wind speeds (Sect. 3.1.3; Bugnard et al., 2025). It suggests that the model may overestimate surface cooling or underestimate turbulent mixing during the evening transition, thereby promoting a stronger and deeper katabatic flow than observed. It possibly also indicates that ICON develops the katabatic layer too rapidly during the evening transition or under-

https://doi.org/10.5194/egusphere-2026-3922
Preprint. Discussion started: 21 July 2026
© Author(s) 2026. CC BY 4.0 License.

estimates the surface drag that would limit its depth and speed in the first hours after onset (Quimbayo-Duarte et al., 2025). Wind directions in the model should also be interpreted cautiously during periods of very weak simulated wind speeds, when directional variability becomes highly sensitive to small velocity errors (He et al., 2023).

After 22:30 UTC, both observations and simulations show the establishment of a well-developed nighttime katabatic flow. This development occurs despite increasing wind speeds at 500 hPa and a transition to northerly synoptic forcing (Fig. A2). This transition is also well represented by ICON. Compared to the other periods during the day, this regime is characterized by a more coherent and less disturbed flow structure, which likely contributes to the improved model performance.

Overall, this case study reveals that ICON-LES captures the dominant flow regimes and their temporal evolution reasonably well, particularly during persistent down-glacier wind and topographically induced westerly flow. The largest discrepancies occur during transition periods when multiple forcing mechanisms interact. Specifically, the model fails to reproduce the unexplained up-valley flow observed between 02:00 and 09:30 UTC and exhibits systematic biases in the simulated depth of the down-glacier wind. These findings highlight that the representation of flow interactions between glacier winds, synoptic forcing, and terrain-induced channeling remains a key challenge, even at high resolutions. They also align with broader assessments of LES performance in mountainous regions, where increasing resolution does not automatically resolve all deficiencies, and turbulence parameterization choices can systematically alter the timing and depth of thermally driven circulations (e.g., Goger and Dipankar, 2024; Schmidli and Quimbayo-Duarte, 2023; Pentikäinen et al., 2023).

Table 4 shows that the selected case study is broadly representative of the model performance for the entire observational period. For wind direction, errors within the lowest 50 m AGL are generally smaller when considering the full campaign than during the selected case study, indicating that the flow complexity observed on 10 August represents a comparatively challenging situation for the model. Above 50 m AGL, error magnitudes are similar, suggesting that the discrepancies identified on the selected day are characteristic of the model's performance under a wide range of atmospheric conditions. In contrast, wind speed errors are slightly larger for the full observational period than for the case study day, indicating that 10 August represents a moderately favorable case in terms of reproducing the observed velocity magnitudes. Nevertheless, the overall consistency between the case study and campaign-wide statistics demonstrates that the strengths and limitations identified from the detailed daily analysis reflect systematic model behavior rather than isolated discrepancies.

The obtained error magnitudes are also comparable to those in previous validation studies based on near-surface observations (e.g., Jiménez and Dudhia, 2013) and lidar-based model evaluations (e.g., Rios et al., 2025), despite these studies employing substantially coarser model resolutions (kilometer scale), larger simulation domains, and generally less heterogeneous flow conditions. This suggests that the simulated flow field performs within the expected uncertainty range for atmospheric simulations over complex terrain.

3.3 Further model limitations and methodological considerations

Accurately simulating glacier boundary layer processes requires appropriate representation of both the underlying topography and surface characteristics. Previous studies have demonstrated that coarse horizontal resolutions are unable to resolve the shallow, stably stratified boundary layer that develops over glacier surfaces, particularly in glacierized valleys (Goger et al.,

https://doi.org/10.5194/egusphere-2026-3922
Preprint. Discussion started: 21 July 2026
© Author(s) 2026. CC BY 4.0 License.

Table 4. Statistical evaluation of WindRanger lidar observations against ICON-LES model output at four vertical levels over the full HEFEX III campaign period. Values in brackets correspond to the selected case study day (10 August 2025). The comparison is based on 3 hour moving window resampling. Equations for the metrics are listed in Appendix A.

Variable	Metric	15 m	50 m	150 m	200 m
number of paired observations (N)		1062 (48)	886 (48)	824 (48)	735 (48)
Wind direction (°)	RMSE	65 (82)	74 (75)	78 (60)	83 (56)
	$\mathrm{RMSE_{rel}}$ (%)	36 (46)	41 (42)	43 (33)	46 (31)
	MAE	45 (58)	55 (61)	57 (45)	61 (40)
Wind speed ($\mathrm{m\ s^{-1}}$)	RMSE	1.34 (1.16)	1.39 (0.88)	1.37 (0.81)	1.88 (1.08)
	MAE	1.02 (0.90)	1.01 (0.77)	1.01 (0.66)	1.31 (0.88)
	MBE	-0.15 (-0.27)	-0.30 (-0.54)	-0.31 (-0.34)	-0.44 (-0.29)

2022). Capturing mountain boundary layer dynamics generally requires at least ten grid points across the glacierized valley width (Wagner et al., 2014), a criterion fulfilled in this study through the use of a 51 m horizontal resolution. Unlike other atmospheric models that employ terrain-following coordinates and therefore require substantial terrain smoothing (e.g., Sauter et al., 2026; Goger et al., 2022), ICON's triangular grid formulation permits the representation of much steeper topography (Zängl et al., 2015). Nevertheless, some limitations in the treatment of complex terrain remain. Most notably, ICON does not account for topographic shading (Prill et al., 2025), despite its strong influence on the surface energy balance (SEB) and the timing of radiative forcing in mountainous environments (Sauter et al., 2026), especially at high resolutions, where steep terrain is explicitly resolved (Chow et al., 2006). The absence of this process likely contributes to timing errors and the remaining biases in near-surface variables. In addition, previous evaluations have shown that ICON operated in LES mode can exhibit excessive turbulent mixing within stable boundary layers (Giovannini et al., 2023), suggesting that alternative turbulence parameterizations may be tested to further improve model performance.

Beyond topographic effects, the representation of glacier surfaces remains another important source of uncertainty. ICON does not explicitly distinguish glacier ice or debris-covered areas from snow-covered surfaces, thereby neglecting substantial spatial variability in surface roughness, albedo, thermal conductivity, and the effects of impurities or supraglacial debris (e.g., Chambers et al., 2021; Collier et al., 2015; Sandu et al., 2013). Such surface properties strongly influence the SEB and, consequently, near-surface atmospheric conditions. Previous studies have demonstrated that more realistic representations of exposed ice and debris-covered surfaces can substantially improve simulated SEB components and increase agreement between modeled and observed meteorological variables (e.g., Potter et al., 2021; Collier et al., 2015). Similar challenges arise from the use of land surface datasets that are often too coarse to adequately resolve complex alpine terrain (Golzio et al., 2021). Although this study employs glacier outlines with substantially higher accuracy than the default external model parameters, the remaining discrepancies indicate that further improvements in surface characterization are required. An additional source of uncertainty is the DEM, which does not fully capture recent glacier thinning and associated topographic changes. Updated

https://doi.org/10.5194/egusphere-2026-3922
Preprint. Discussion started: 21 July 2026
© Author(s) 2026. CC BY 4.0 License.

high-resolution DEMs that better represent the current glacier surface could further improve the representation of near-surface flow and local thermodynamic forcing.

The observational framework used in this study provides a comprehensive basis for evaluating model performance. The combination of UAV-based observations and Doppler lidar measurements enables an assessment of both the thermodynamic structure and wind field within the valley atmosphere (Gaffey and Bhardwaj, 2020). However, the observations themselves are subject to methodological uncertainties that must be considered when interpreting model–observation differences. In particular, lidar retrievals generally assume horizontally homogeneous flow conditions, an assumption that is rarely satisfied in glacierized mountain valleys characterized by strong terrain-induced flow distortions (Pentikäinen et al., 2023). Nevertheless, the dataset offers a rare opportunity to evaluate model performance under realistic atmospheric conditions. Previous studies have reported uncertainties of approximately 5–10 $\%$ in lidar-derived mean wind speeds arising from factors such as terrain complexity, surface roughness, atmospheric stability, measurement height, and lidar scan geometry (Courtney et al., 2008). These uncertainties should therefore be considered when assessing residual discrepancies between the simulations and observations (Klaas-Witt and Emeis, 2022).

4 Summary and conclusion

The validation presented in this study uses an exceptionally comprehensive observational dataset over a glacier, providing a robust basis for evaluating ICON-LES at 51 m horizontal resolution in a highly complex alpine environment. The dataset spans 48 days of measurements from 22 stations distributed across glacier, forefield, and surrounding terrain, covering two field campaigns multiscale2025. It is strengthened by a dense on-glacier observational system that combines automatic weather stations, a 10 m instrumented tower, two Doppler lidar systems, and UAV-based profiles at multiple locations. Together, these observations enable a multiscale evaluation of near-surface and lower-atmospheric processes that are rarely accessible in steep terrain.

Across the full dataset, ICON-LES reproduces the large-scale spatial structure of temperature, humidity, and wind fields with good fidelity. Near-surface air temperature shows realistic elevation-dependent gradients across the glacier, indicating a generally well-represented surface–atmosphere coupling. Deviations are primarily temporal rather than spatial. A modest warm bias occurs near the surface under undisturbed katabatic conditions, while a slight cold bias appears in the broader valley atmosphere when evaluated against UAV-derived profiles and near the surface during well-mixed conditions. These opposing biases point to processes acting within the lowest few meters above the surface, including unresolved shallow inversions and katabatic jet structures, rather than fundamental deficiencies in the resolved atmospheric dynamics.

Wind observations from the WindRanger and StreamLine Doppler lidar systems show that ICON-LES captures the dominant flow patterns over the glacier–valley system. However, model performance decreases when multiple forcing mechanisms interact, including terrain-induced channeling and other orographic effects. In these situations, transitions between thermally driven katabatic flow and dynamically forced valley-scale winds are smoother in the model than in the observations. RHI scans further indicate that the simulated katabatic layer is too diffuse, particularly during periods with opposing synoptic flow

https://doi.org/10.5194/egusphere-2026-3922
Preprint. Discussion started: 21 July 2026
© Author(s) 2026. CC BY 4.0 License.

aloft, which weakens the observed vertical decoupling between the glacier boundary layer and the flow aloft. These limitations become most apparent when small shifts in stability and pressure gradients strongly control near-surface wind structure.

The timing differences in flow transitions further suggest sensitivity to land surface representation, including debris cover, bare ice parameterization, and topographic shading. These factors are not yet explicitly represented, but they likely influence surface energy partitioning. Despite these limitations, the simulations show remarkably small systematic biases, demonstrating their robustness in complex terrain.

The model provides spatially continuous fields of meteorological variables that are now evaluated against an extensive independent observational dataset. This provides a solid basis for process-oriented analyses of atmosphere–glacier interactions, including katabatic flow dynamics and valley-scale circulation coupling. Future work should focus on targeted sensitivity experiments to assess the conditions under which glaciers can maintain their microclimate and how retreating glaciers interact with the valley atmosphere and beyond. The present setup also enables future coupling of ICON-LES to higher-resolution near-surface modeling frameworks, which could improve the representation of shallow stability-driven flows, surface heterogeneity, and sub-meter-scale turbulence processes that remain unresolved at 51 m grid spacing. These efforts should be extended across seasons, synoptic conditions, and additional alpine sites to improve generality. Together, they will strengthen confidence in using ICON-LES for studying coupled land–atmosphere processes in complex terrain.

Code and data availability. The numerical simulations presented in this study were performed using version 2024.10 of the ICOsahedral Nonhydrostatic model (ICON; DOI:10.35089/WDCC/IconRelease2024.10; ICON partnership (DWD, MPI-M, DKRZ, KIT, C2SM), 2024).

The data analysis and visualization in this study were performed using Python scripts developed by the main author. The scripts used to process and analyze the datasets have been published on Zenodo (DOI:10.5281/zenodo.21224549; Georgi, 2026a).

Data needed to reproduce the analysis and derived analysis products supporting all figures and tables in this study are archived on Zenodo along with our customized ICON grids and external parameter files (DOI:10.5281/zenodo.19603818; Georgi and Sauter, 2026).

Observations and corresponding ICON data from HEFEX II AWSs (DOI:10.5281/zenodo.21130355; Georgi, 2026b), HEFEX III AWSs (DOI:10.5281/zenodo.21130441; Georgi, 2026c), UAV profiles (DOI:10.5281/zenodo.19596612; Georgi, 2026d), StreamLine Doppler lidar (DOI:10.5281/zenodo.19626880; Georgi and Springer, 2026), and WindRanger Doppler lidar (DOI:10.5281/zenodo.19596272; Georgi, 2026e).

All datasets are available under open-access licenses, unless otherwise noted.

Appendix A: Verification metrics

To evaluate the agreement between simulated and observed wind variables, we calculate error statistics for both wind direction and wind speed. Because wind direction is a circular variable, the directional error is first computed as the minimum angular

https://doi.org/10.5194/egusphere-2026-3922
Preprint. Discussion started: 21 July 2026
© Author(s) 2026. CC BY 4.0 License.

distance accounting for the periodicity of 360°:

$$\Delta d_i = \min\Big(|d_{i,\mathrm{ICON}} - d_{i,\mathrm{obs}}|, \\ |d_{i,\mathrm{ICON}} - d_{i,\mathrm{obs}} - 360^\circ|, \\ |d_{i,\mathrm{ICON}} - d_{i,\mathrm{obs}} + 360^\circ| \Big) \tag{A1}$$

where Δd_i denotes the absolute directional error for sample i.

The root mean square error (RMSE) of wind direction is:

$$\mathrm{RMSE}_{\mathrm{dir}} = \sqrt{\frac{1}{N}\sum_{i=1}^{N}(\Delta d_i)^2} \tag{A2}$$

The relative RMSE of wind direction (normalized by 180°) is:

$$\mathrm{RMSE}_{\mathrm{dir,rel}} = \frac{\mathrm{RMSE}_{\mathrm{dir}}}{180^\circ} \times 100 \tag{A3}$$

The mean absolute error (MAE) of wind direction is:

$$\mathrm{MAE}_{\mathrm{dir}} = \frac{1}{N}\sum_{i=1}^{N}\Delta d_i \tag{A4}$$

Wind speed RMSE is defined as:

$$\mathrm{RMSE}_{\mathrm{spd}} = \sqrt{\frac{1}{N}\sum_{i=1}^{N}(U_{i,\mathrm{ICON}} - U_{i,\mathrm{obs}})^2} \tag{A5}$$

Wind speed MAE is:

$$\mathrm{MAE}_{\mathrm{spd}} = \frac{1}{N}\sum_{i=1}^{N}|U_{i,\mathrm{ICON}} - U_{i,\mathrm{obs}}| \tag{A6}$$

The mean bias error (MBE) of wind speed is:

$$\mathrm{MBE}_{\mathrm{spd}} = \frac{1}{N}\sum_{i=1}^{N}(U_{i,\mathrm{ICON}} - U_{i,\mathrm{obs}}) \tag{A7}$$

where N is the number of paired samples, d_{ICON} and d_{obs} are modeled and observed wind directions in degrees, and U_{ICON} and U_{obs} are modeled and observed wind speeds in $\mathrm{m\,s^{-1}}$.

Author contributions. TS and AG configured the ICON model. AG performed the simulations. TS, AG, and LN contributed to HEFEX II, all authors contributed to HEFEX III. AG conducted all the analyses, developed the analysis code, and wrote the original manuscript. MS contributed to lidar data processing. TS, KFH, and LS reviewed and edited the manuscript. TS and LN acquired funding.

https://doi.org/10.5194/egusphere-2026-3922
Preprint. Discussion started: 21 July 2026
© Author(s) 2026. CC BY 4.0 License.

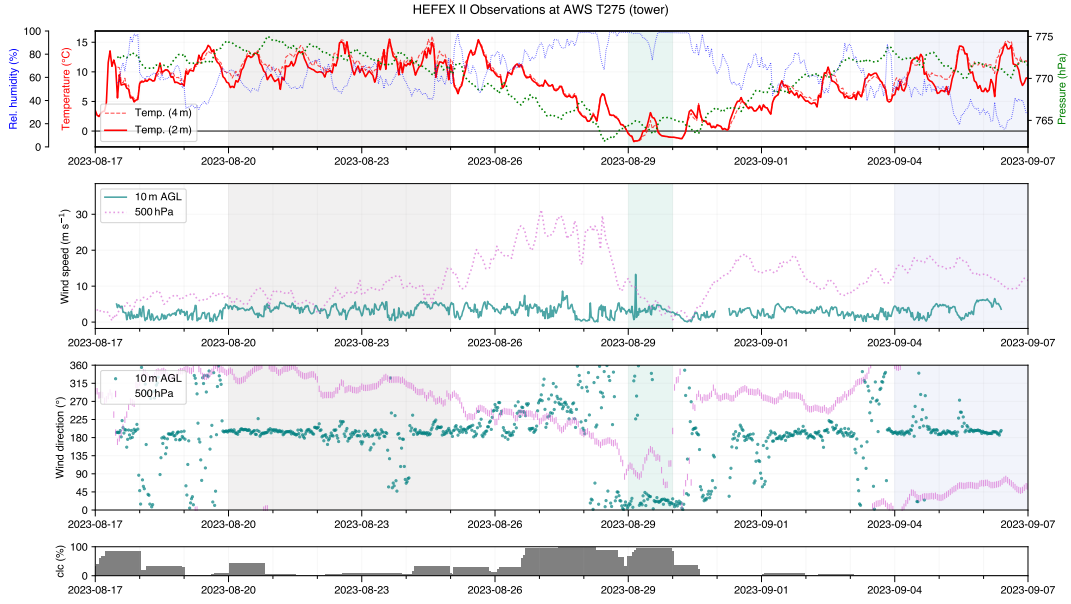

Figure A1. Temporal evolution of meteorological conditions during the HEFEX II campaign period. Panels show observed near-surface air temperature at 2 m and 4 m AGL, relative humidity, surface pressure, and wind conditions measured at station T275. In addition, large-scale atmospheric conditions are represented by wind conditions at the 500 hPa level and fraction of cloud cover derived from ERA5 reanalysis data (Hersbach et al., 2023). Shaded periods indicate the selected time intervals analyzed in Sect. 3.1.3 to assess model performance under different local flow regimes and varying synoptic forcing conditions (Fig. 3).

Competing interests. The authors declare that they have no conflict of interest.

Acknowledgements. This work used resources from the Deutsches Klimarechenzentrum (DKRZ) granted by its Scientific Steering Committee (WLA) under project ID 1461 *Glacier Space*.

The following AI tools were used to prepare this manuscript: Claude (https://claude.ai) and Consensus.app (https://consensus.app) for literature research and summaries, DeepL Write (https://www.deepl.com/write) and ChatGPT 4o (https://openai.com/chatgpt) for grammar and spelling checks, and rephrasing.

Financial support. This research was funded by a DFG-FWF WEAVE Grant (DFG Grant Agreement No. 543257843; FWF Grant-DOI 10.55776/PIN1775223).

The article processing charges for this open-access publication were covered by the Humboldt-Universität zu Berlin.

https://doi.org/10.5194/egusphere-2026-3922
Preprint. Discussion started: 21 July 2026
© Author(s) 2026. CC BY 4.0 License.

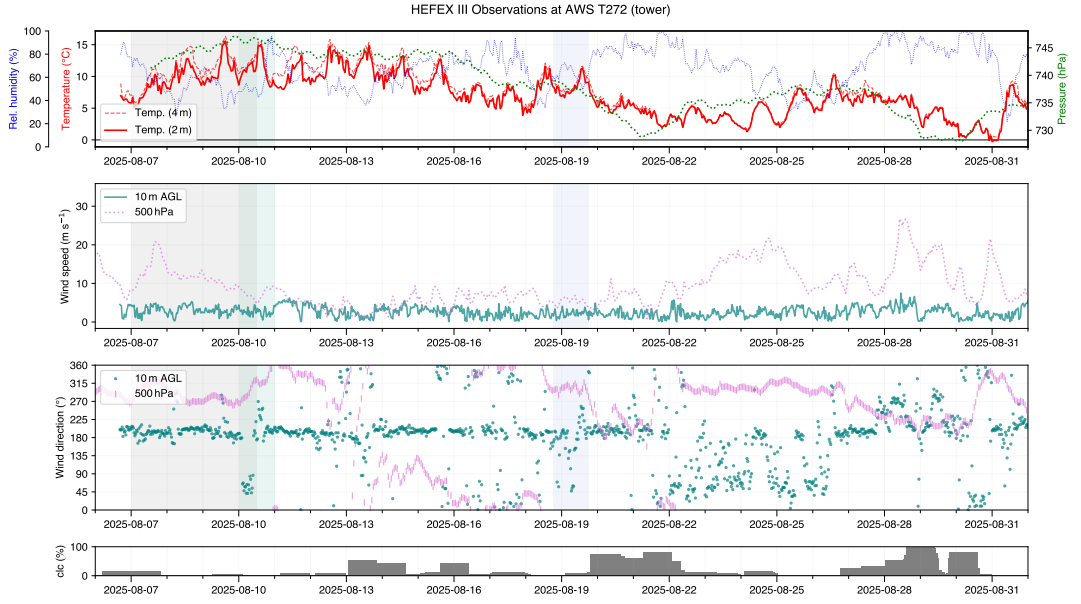

Figure A2. Temporal evolution of meteorological conditions during the HEFEX III campaign period. Panels show observed near-surface air temperature at 2 m and 4 m AGL, relative humidity, surface pressure, and wind conditions measured at station T272. In addition, large-scale atmospheric conditions are represented by wind conditions at the 500 hPa level and fraction of cloud cover derived from ERA5 reanalysis data (Hersbach et al., 2023). Shaded periods indicate the selected intervals analyzed in this study, including both IOPs used for evaluation against UAV sounding measurements in gray and blue (Sect. 3.2.1; Table 3) and the case study period used for the detailed analysis of in-valley flow structures based on Doppler lidar observations in green (Sect. 3.2.2; Fig. 5 and 6).

References

Arino, O., Ramos Perez, J. J., Kalogirou, V., Bontemps, S., Defourny, P., and Van Bogaert, E.: Global Land Cover Map for 2009 (GlobCover 2009), https://doi.org/10.1594/PANGAEA.787668, 2012.

ASTER Science Team: ASTER Global Digital Elevation Model V003, https://doi.org/https://doi.org/10.5067/ASTER/ASTGTM.003, 2019.

Bugnard, A., Collaud Coen, M., Hervo, M., Leuenberger, D., Arpagaus, M., and Monhart, S.: Comparison of Temperature and Wind Profiles between Ground-Based Remote Sensing Observations and Numerical Weather Prediction Model in Complex Alpine Topography: The Meiringen Campaign, Atmospheric Measurement Techniques, 18, 1039–1061, https://doi.org/10.5194/amt-18-1039-2025, 2025.

Casasanta, G., Conte, M., Sozzi, R., Cecilia, A., Petenko, I., and Argentini, S.: Towards Definitive Functional Forms for Monin–Obukhov Similarity Functions in Stable and Very Stable Surface Layers, Scientific Reports, 15, 25 632, https://doi.org/10.1038/s41598-025-10815-3, 2025.

Chambers, J. R., Smith, M. W., Smith, T., Sailer, R., Quincey, D. J., Carrivick, J. L., Nicholson, L., Mertes, J., Stiperski, I., and James, M. R.: Correcting for Systematic Underestimation of Topographic Glacier Aerodynamic Roughness Values From Hintereisferner, Austria, Frontiers in Earth Science, 9, 691 195, https://doi.org/10.3389/feart.2021.691195, 2021.

https://doi.org/10.5194/egusphere-2026-3922
Preprint. Discussion started: 21 July 2026
© Author(s) 2026. CC BY 4.0 License.

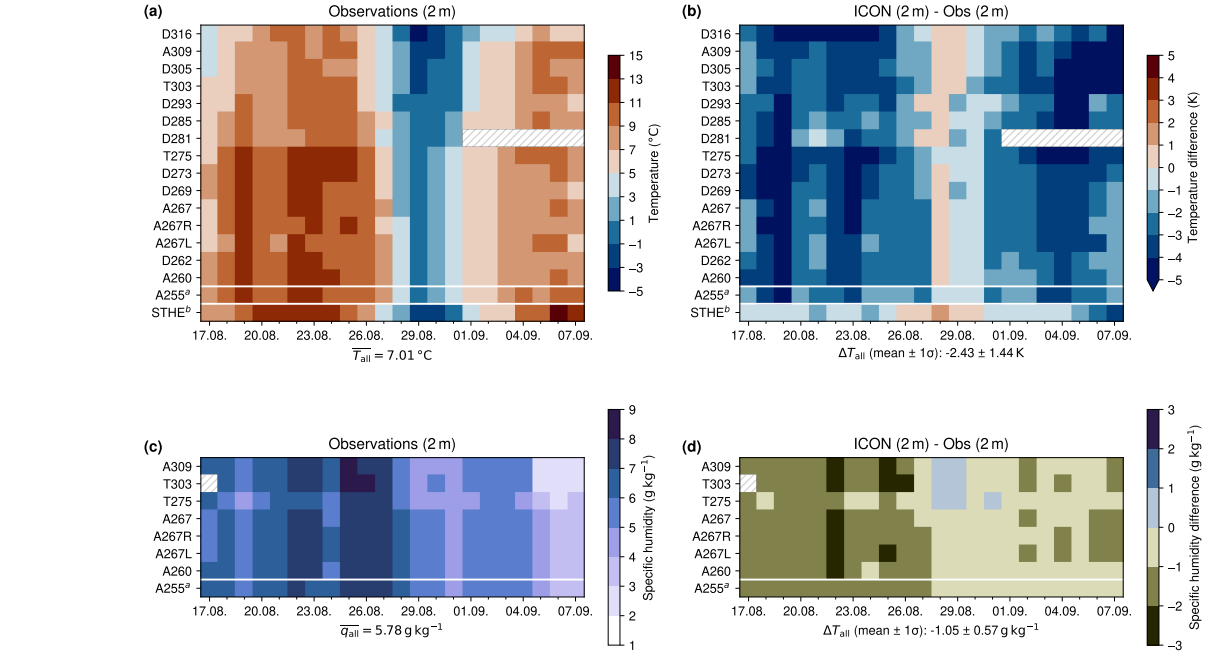

Figure A3. Same as Fig. 2, but using diagnostic 2 m ICON output instead of prognostic model output at 5 m.

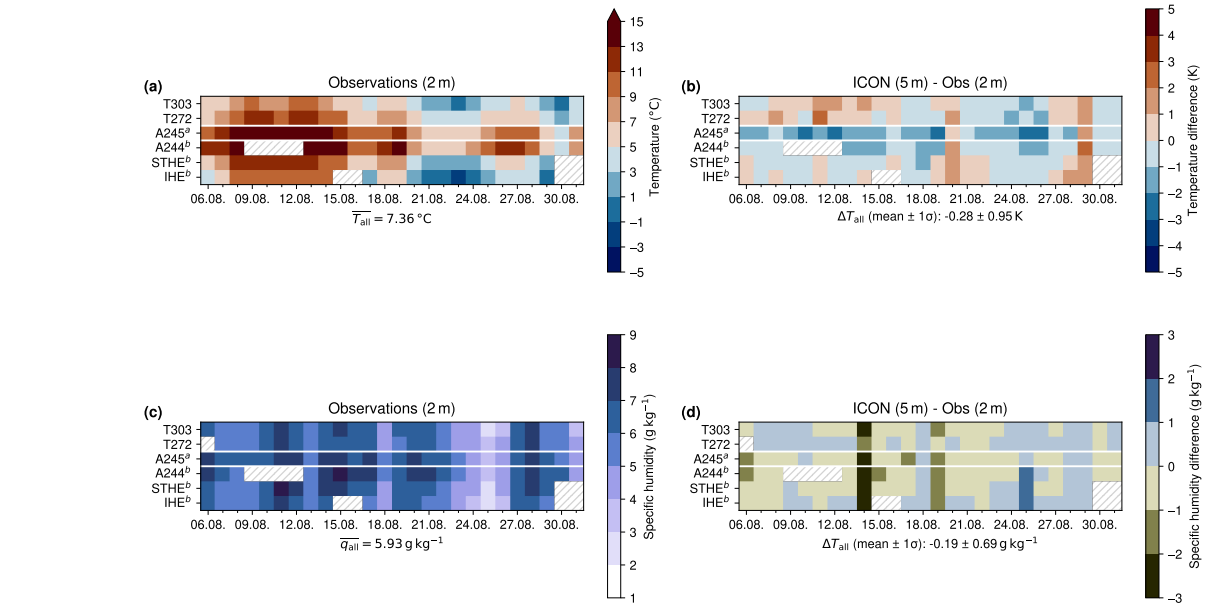

Figure A4. Same as Fig. 2, but comparing observational and simulated data from the HEFEX III campaign period.

Chow, F. K., Weigel, A. P., Street, R. L., Rotach, M. W., and Xue, M.: High-Resolution Large-Eddy Simulations of Flow in a Steep Alpine Valley. Part I: Methodology, Verification, and Sensitivity Experiments, Journal of Applied Meteorology and Climatology, 45, 63–86, https://doi.org/10.1175/JAM2322.1, 2006.

https://doi.org/10.5194/egusphere-2026-3922
Preprint. Discussion started: 21 July 2026
© Author(s) 2026. CC BY 4.0 License.

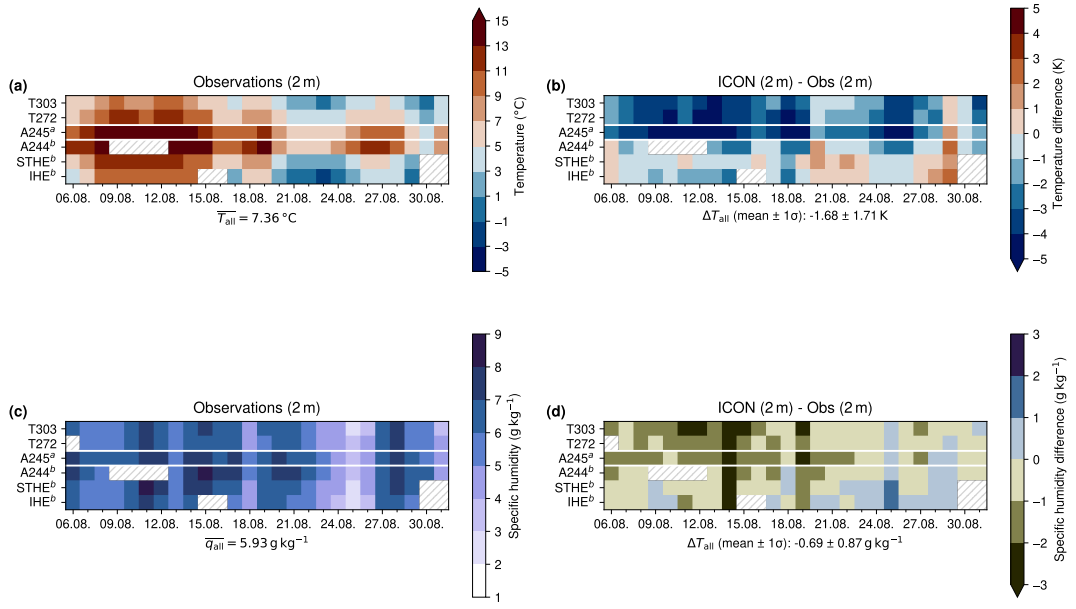

Figure A5. Same as Fig. A4, but using diagnostic 2 m ICON output instead of prognostic model output at 5 m.

Collier, E., Maussion, F., Nicholson, L. I., Mölg, T., Immerzeel, W. W., and Bush, A. B. G.: Impact of Debris Cover on Glacier Ablation and Atmosphere–Glacier Feedbacks in the Karakoram, The Cryosphere, 9, 1617–1632, https://doi.org/10.5194/tc-9-1617-2015, 2015.

Conway, J. and Cullen, N.: Constraining Turbulent Heat Flux Parameterization over a Temperate Maritime Glacier in New Zealand, Annals of Glaciology, 54, 41–51, https://doi.org/10.3189/2013AoG63A604, 2013.

Courtney, M., Wagner, R., and Lindelöw, P.: Testing and Comparison of Lidars for Profile and Turbulence Measurements in Wind Energy, IOP Conference Series: Earth and Environmental Science, 1, 012 021, https://doi.org/10.1088/1755-1315/1/1/012021, 2008.

Cuxart, J.: When Can a High-Resolution Simulation Over Complex Terrain Be Called LES?, Frontiers in Earth Science, 3, https://doi.org/10.3389/feart.2015.00087, 2015.

Deutscher Wetterdienst: Deutscher Wetterdienst: PArallel MOdel data REtrieve from Oracle databases (PAMORE), https://www.dwd.de/DE/leistungen/pamore/pamore.html, (last access: 30 June 2026), 2026.

Dipankar, A., Stevens, B., Heinze, R., Moseley, C., Zängl, G., Giorgetta, M., and Brdar, S.: Large Eddy Simulation Using the General Circulation Model ICON, Journal of Advances in Modeling Earth Systems, 7, 963–986, https://doi.org/10.1002/2015MS000431, 2015.

Gaffey, C. and Bhardwaj, A.: Applications of Unmanned Aerial Vehicles in Cryosphere: Latest Advances and Prospects, Remote Sensing, 12, 948, https://doi.org/10.3390/rs12060948, 2020.

Georgi, A.: ClimLabTools/icon_validation: v1.0 - Initial release ICON validation notebooks, https://doi.org/10.5281/zenodo.21224549, 2026a.

Georgi, A.: HEFEX II: Automatic Weather Station observations and ICON-LES simulations at Hintereisferner glacier (Austria), https://doi.org/10.5281/zenodo.21130355, 2026b.

Georgi, A.: HEFEX III: Automatic Weather Station observations and ICON-LES simulations at Hintereisferner glacier (Austria), https://doi.org/doi.org/10.5281/zenodo.21130441, 2026c.

https://doi.org/10.5194/egusphere-2026-3922
Preprint. Discussion started: 21 July 2026
© Author(s) 2026. CC BY 4.0 License.

Georgi, A.: HEFEX III: UAV atmospheric profiles and ICON-LES simulations at Hintereisferner glacier (Austria), https://doi.org/10.5281/zenodo.19596612, 2026d.

Georgi, A.: HEFEX III: WindRanger Doppler lidar observations and ICON-LES simulations at Hintereisferner glacier (Austria), https://doi.org/10.5281/zenodo.19596272, 2026e.

Georgi, A. and Sauter, T.: ICON model domains and external parameter files for glacier evolution experiments at Hintereisferner (Austria), https://doi.org/10.5281/zenodo.19603818, 2026.

Georgi, A. and Springer, M.: HEFEX III: Doppler lidar RHI scans and projected ICON-LES outputs at Hintereisferner glacier (Austria), https://doi.org/10.5281/zenodo.19626880, 2026.

Giovannini, L., Bazile, E., Deidda, P., Ferrarese, S., Ferrero, E., Goger, B., Gohm, A., Golzio, A., Honnert, R., Köhler, M., Oettl, D., Pauly, L., Rodier, Q., Schmidli, J., Seity, Y., Serafin, S., Sheridan, P., Singh, S., Trini Castelli, S., Wastl, C., Westerhuis, S., and Zonato, A.: A Model Intercomparison Study of the Thermally-Driven Wind System in an Alpine Valley, https://doi.org/10.3929/ETHZ-B-000618961, 2023.

Goger, B. and Dipankar, A.: The Impact of Mesh Size, Turbulence Parameterization, and Land-surface-exchange Scheme on Simulations of the Mountain Boundary Layer in the Hectometric Range, Quarterly Journal of the Royal Meteorological Society, 150, 3853–3873, https://doi.org/10.1002/qj.4799, 2024.

Goger, B., Stiperski, I., Nicholson, L., and Sauter, T.: Large-eddy Simulations of the Atmospheric Boundary Layer over an Alpine Glacier: Impact of Synoptic Flow Direction and Governing Processes, Quarterly Journal of the Royal Meteorological Society, 148, 1319–1343, https://doi.org/10.1002/qj.4263, 2022.

Golzio, A., Ferrarese, S., Cassardo, C., Diolaiuti, G. A., and Pelfini, M.: Land-Use Improvements in the Weather Research and Forecasting Model over Complex Mountainous Terrain and Comparison of Different Grid Sizes, Boundary-Layer Meteorology, 180, 319–351, https://doi.org/10.1007/s10546-021-00617-1, 2021.

Greene, B. R., Segales, A. R., Bell, T. M., Pillar-Little, E. A., and Chilson, P. B.: Environmental and Sensor Integration Influences on Temperature Measurements by Rotary-Wing Unmanned Aircraft Systems, Sensors, 19, 1470, https://doi.org/10.3390/s19061470, 2019.

Groos, A. R., Brand, N., Bronz, M., and Philipp, A.: Atmospheric Sounding of the Boundary Layer over Alpine Glaciers Using Fixed-Wing UAVs, Atmospheric Measurement Techniques, 18, 6493–6512, https://doi.org/10.5194/amt-18-6493-2025, 2025.

Gutjahr, O., Putrasahan, D., Lohmann, K., Jungclaus, J. H., Von Storch, J.-S., Brüggemann, N., Haak, H., and Stössel, A.: Max Planck Institute Earth System Model (MPI-ESM1.2) for the High-Resolution Model Intercomparison Project (HighResMIP), Geoscientific Model Development, 12, 3241–3281, https://doi.org/10.5194/gmd-12-3241-2019, 2019.

Hansche, I., Shahi, S., Abermann, J., and Schöner, W.: The Vertical Atmospheric Structure of the Partially Glacierised Mittivakkat Valley, Southeast Greenland, Journal of Glaciology, 69, 1097–1108, https://doi.org/10.1017/jog.2022.120, 2023.

Hattenberger, G., Bronz, M., and Gorraz, M.: Using the Paparazzi UAV System for Scientific Research, in: IMAV 2014: International Micro Air Vehicle Conference and Competition, Delft University of Technology, https://doi.org/10.4233/UUID:B38FBDB7-E6BD-440D-93BE-F7DD1457BE60, 2014.

Haualand, K. F., Sauter, T., Abermann, J., De Villiers, S. D., Georgi, A., Goger, B., Dawson, I., Nerhus, S. D., Robson, B. A., Sjursen, K. H., Thomas, D. J., Thomaser, M., and Yde, J. C.: Meteorological Impact of Glacier Retreat and Proglacial Lake Temperature in Western Norway, Journal of Geophysical Research: Atmospheres, 130, e2024JD042 715, https://doi.org/10.1029/2024JD042715, 2025.

https://doi.org/10.5194/egusphere-2026-3922
Preprint. Discussion started: 21 July 2026
© Author(s) 2026. CC BY 4.0 License.

He, Y., Han, X., Xu, C., Cheng, Z., Wang, J., Liu, W., and Xu, D.: Sensitivity of Simulated Wind Power under Diverse Spatial Scales and Multiple Terrains Using the Weather Research and Forecasting Model, Energy, 285, 129 430, https://doi.org/10.1016/j.energy.2023.129430, 2023.

Heinze, R., Dipankar, A., Henken, C. C., Moseley, C., Sourdeval, O., Trömel, S., Xie, X., Adamidis, P., Ament, F., Baars, H., Barthlott, C., Behrendt, A., Blahak, U., Bley, S., Brdar, S., Brueck, M., Crewell, S., Deneke, H., Di Girolamo, P., Evaristo, R., Fischer, J., Frank, C., Friederichs, P., Göcke, T., Gorges, K., Hande, L., Hanke, M., Hansen, A., Hege, H.-C., Hoose, C., Jahns, T., Kalthoff, N., Klocke, D., Kneifel, S., Knippertz, P., Kuhn, A., Van Laar, T., Macke, A., Maurer, V., Mayer, B., Meyer, C. I., Muppa, S. K., Neggers, R. A. J., Orlandi, E., Pantillon, F., Pospichal, B., Röber, N., Scheck, L., Seifert, A., Seifert, P., Senf, F., Siligam, P., Simmer, C., Steinke, S., Stevens, B., Wapler, K., Weniger, M., Wulfmeyer, V., Zängl, G., Zhang, D., and Quaas, J.: Large-eddy Simulations over Germany Using ICON: A Comprehensive Evaluation, Quarterly Journal of the Royal Meteorological Society, 143, 69–100, https://doi.org/10.1002/qj.2947, 2017.

Heise, E., Ritter, B., and Schrodin, R.: Operational Implementation of the Multilayer Soil Model, Technical Report 9, DWD, 2006.

Hersbach, H., Bell, B., Berrisford, P., Biavati, G., Horányi, A., Muñoz Sabater, J., Nicolas, J., Peubey, C., Radu, R., Rozum, I., Schepers, D., Simmons, A., Soci, C., Dee, D., and Thépaut, J.-N.: ERA5 hourly data on pressure levels from 1940 to present, https://doi.org/10.24381/cds.bd0915c6, (last access: 16 June 2026), 2023.

Hock, R.: Glacier Melt: A Review of Processes and Their Modelling, Progress in Physical Geography: Earth and Environment, 29, 362–391, https://doi.org/10.1191/0309133305pp453ra, 2005.

ICON partnership (DWD, MPI-M, DKRZ, KIT, C2SM): ICON release 2024.10, https://doi.org/10.35089/WDCC/IconRelease2024.10, 2024.

Jiménez, P. A. and Dudhia, J.: On the Ability of the WRF Model to Reproduce the Surface Wind Direction over Complex Terrain, Journal of Applied Meteorology and Climatology, 52, 1610–1617, https://doi.org/10.1175/JAMC-D-12-0266.1, 2013.

Kimball, S. K., Montalvo, C. J., and Mulekar, M. S.: Assessing iMET-XQ Performance and Optimal Placement on a Small Off-the-Shelf, Rotary-Wing UAV, as a Function of Atmospheric Conditions, Atmosphere, 11, 660, https://doi.org/10.3390/atmos11060660, 2020a.

Kimball, S. K., Montalvo, C. J., and Mulekar, M. S.: Evaluating Temperature Measurements of the iMET-XQ, in the Field, under Varying Atmospheric Conditions, Atmosphere, 11, 335, https://doi.org/10.3390/atmos11040335, 2020b.

Klaas-Witt, T. and Emeis, S.: The Five Main Influencing Factors for Lidar Errors in Complex Terrain, Wind Energy Science, 7, 413–431, https://doi.org/10.5194/wes-7-413-2022, 2022.

Kuhn, M., Dreiseitl, E., Hofinger, S., Markl, G., Span, N., and Kaser, G.: Measurements and Models of the Mass Balance of Hintereisferner, Geografiska Annaler, Series A: Physical Geography, 81, 659–670, https://doi.org/10.1111/j.0435-3676.1999.00094.x, 1999.

Lange, S.: Trend-Preserving Bias Adjustment and Statistical Downscaling with ISIMIP3BASD (v1.0), Geoscientific Model Development, 12, 3055–3070, https://doi.org/10.5194/gmd-12-3055-2019, 2019.

Lehner, M. and Rotach, M. W.: Current Challenges in Understanding and Predicting Transport and Exchange in the Atmosphere over Mountainous Terrain, Atmosphere, 9, 276, https://doi.org/10.3390/atmos9070276, 2018.

Lilly, D. K.: On the Numerical Simulation of Buoyant Convection, Tellus, 14, 148–172, https://doi.org/10.1111/j.2153-3490.1962.tb00128.x, 1962.

Mahrt, L.: Stably Stratified Atmospheric Boundary Layers, Annual Review of Fluid Mechanics, 46, 23–45, https://doi.org/10.1146/annurev-fluid-010313-141354, 2014.

Maronga, B., Knigge, C., and Raasch, S.: An Improved Surface Boundary Condition for Large-Eddy Simulations Based on Monin–Obukhov Similarity Theory: Evaluation and Consequences for Grid Convergence in Neutral and Stable Conditions, Boundary-Layer Meteorology, 174, 297–325, https://doi.org/10.1007/s10546-019-00485-w, 2020.

https://doi.org/10.5194/egusphere-2026-3922
Preprint. Discussion started: 21 July 2026
© Author(s) 2026. CC BY 4.0 License.

Maussion, F., Butenko, A., Champollion, N., Dusch, M., Eis, J., Fourteau, K., Gregor, P., Jarosch, A. H., Landmann, J., Oesterle, F., Recinos, B., Rothenpieler, T., Vlug, A., Wild, C. T., and Marzeion, B.: The Open Global Glacier Model (OGGM) v1.1, Geoscientific Model Development, 2019, 909–931, https://doi.org/10.5194/gmd-12-909-2019, 2019.

Mlawer, E. J., Taubman, S. J., Brown, P. D., Iacono, M. J., and Clough, S. A.: Radiative Transfer for Inhomogeneous Atmospheres: RRTM, a Validated Correlated-k Model for the Longwave, Journal of Geophysical Research: Atmospheres, 102, 16 663–16 682, https://doi.org/10.1029/97JD00237, 1997.

Mott, R., Stiperski, I., and Nicholson, L.: Spatio-Temporal Flow Variations Driving Heat Exchange Processes at a Mountain Glacier, The Cryosphere, 14, 4699–4718, https://doi.org/10.5194/tc-14-4699-2020, 2020.

Mott, R., Haugeneder, M., Stiperski, I., Asemann, P., Reynolds, D., and Nicholson, L.: Characterization of the Near-Surface Air Temperature Dynamics over Glaciers Using Thermal Infrared Measurements, Frontiers in Earth Science, 13, 1658 491, https://doi.org/10.3389/feart.2025.1658491, 2025.

Nicholson, L., Stiperski, I., Nitti, G., Prinz, R., Georgi, A., Groos, A. R., Shaw, T. E., Sauter, T., Haugeneder, M., Mott, R., Sicart, J.-E., Brock, B. W., Albers, R., Allegri, B., Barral, H., Biron, R., Charrondiere, C., Coulaud, C., Fischer, A., Reynolds, D., Richter, N., Schroeder, M., Vettori, P., Voordendag, A., and Wydra, C.: The second HinterEisFerner EXperiment (HEFEX II): Initial insights into boundary layer structure and surface-atmosphere exchange processes from intensive observations at a valley glacier, Bulletin of the American Meteorological Society, 106, E2143 – E2169, https://doi.org/10.1175/BAMS-D-24-0010.1, 2025.

Oerlemans, J.: The Microclimate of Valley Glaciers, Igitur, Universiteitsbibliotheek Utrecht, 2010.

Oerlemans, J. and Grisogono, B.: Glacier Winds and Parameterisation of the Related Surface Heat Fluxes, Tellus A: Dynamic Meteorology and Oceanography, 54, 440, https://doi.org/10.3402/tellusa.v54i5.12164, 2002.

Pentikäinen, P., O'Connor, E. J., and Ortiz-Amezcua, P.: Evaluating Wind Profiles in a Numerical Weather Prediction Model with Doppler Lidar, Geoscientific Model Development, 16, 2077–2094, https://doi.org/10.5194/gmd-16-2077-2023, 2023.

Potter, E. R., Orr, A., Willis, I. C., Bannister, D., and Wagnon, P.: Meteorological Impacts of a Novel Debris-covered Glacier Category in a Regional Climate Model across a Himalayan Catchment, Atmospheric Science Letters, 22, e1018, https://doi.org/10.1002/asl.1018, 2021.

Prill, F., Reinert, D., Rieger, D., and Zängl, G.: ICON Tutorial 2025: Working with the ICON Model, https://doi.org/10.5676/DWD_PUB/NWV/ICON_TUTORIAL2025, 2025.

Quimbayo-Duarte, J., Schmidli, J., Köhler, M., and Schlemmer, L.: Analysis of the Wind Response to Resolved versus Parametrized Turbulent Orographic Drag in High-resolution Simulations, Quarterly Journal of the Royal Meteorological Society, 151, e4977, https://doi.org/10.1002/qj.4977, 2025.

Raschendorfer, M.: The New Turbulence Parameterization of LM, Newsletter 1, Consortium for Small-Scale Modelling, 2001.

Rios, G., Arthur, R. S., Wharton, S., and Fast, J. D.: Lidar-Based Evaluation of HRRR Performance in California's Diablo Range, Weather and Forecasting, 40, 1935–1952, https://doi.org/10.1175/WAF-D-24-0146.1, 2025.

Rotach, M. W., Serafin, S., Ward, H. C., Arpagaus, M., Colfescu, I., Cuxart, J., De Wekker, S. F. J., Grubišic, V., Kalthoff, N., Karl, T., Kirshbaum, D. J., Lehner, M., Mobbs, S., Paci, A., Palazzi, E., Bailey, A., Schmidli, J., Wittmann, C., Wohlfahrt, G., and Zardi, D.: A Collaborative Effort to Better Understand, Measure, and Model Atmospheric Exchange Processes over Mountains, Bulletin of the American Meteorological Society, 103, E1282–E1295, https://doi.org/10.1175/BAMS-D-21-0232.1, 2022.

Salerno, F., Guyennon, N., Yang, K., Shaw, T. E., Lin, C., Colombo, N., Romano, E., Gruber, S., Bolch, T., Alessandri, A., Cristofanelli, P., Putero, D., Diolaiuti, G., Tartari, G., Verza, G., Thakuri, S., Balsamo, G., Miles, E. S., and Pellicciotti, F.: Local Cooling and Drying

https://doi.org/10.5194/egusphere-2026-3922
Preprint. Discussion started: 21 July 2026
© Author(s) 2026. CC BY 4.0 License.

Induced by Himalayan Glaciers under Global Warming, Nature Geoscience, 16, 1120–1127, https://doi.org/10.1038/s41561-023-01331-y, 2023.

Sandu, I., Beljaars, A., Bechtold, P., Mauritsen, T., and Balsamo, G.: Why Is It so Difficult to Represent Stably Stratified Conditions in Numerical Weather Prediction (NWP) Models?, Journal of Advances in Modeling Earth Systems, 5, 117–133, https://doi.org/10.1002/jame.20013, 2013.

Sauter, T. and Galos, S. P.: Effects of Local Advection on the Spatial Sensible Heat Flux Variation on a Mountain Glacier, The Cryosphere, 10, 2887–2905, https://doi.org/10.5194/tc-10-2887-2016, 2016.

Sauter, T., Brock, B. W., Collier, E., Goger, B., Groos, A. R., Haualand, K. F., Mott, R., Nicholson, L., Prinz, R., Shaw, T. E., Stiperski, I., Georgi, A., Haugeneder, M., Mandal, A., Reynolds, D., Saigger, M., Sicart, J. E., and Voordendag, A.: Glacier-Atmosphere Interactions and Feedbacks in High-Mountain Regions - A Review, Reviews of Geophysics, 64, e2024RG000 869, https://doi.org/10.1029/2024RG000869, 2026.

Schaaf, C. and Wang, Z.: MODIS/Terra+Aqua BRDF/Albedo Daily L3 Global - 500m V061, https://doi.org/10.5067/MODIS/MCD43A3.061, 2021.

Schmidli, J. and Quimbayo-Duarte, J.: Diurnal Valley Winds in a Deep Alpine Valley: Model Results, Meteorology, 2, 87–106, https://doi.org/10.3390/meteorology2010007, 2023.

Schulz, J.-P. and Vogel, G.: Improving the Processes in the Land Surface Scheme TERRA: Bare Soil Evaporation and Skin Temperature, Atmosphere, 11, 513, https://doi.org/10.3390/atmos11050513, 2020.

Schulz, J.-P., Vogel, G., Becker, C., Kothe, S., Rummel, U., and Ahrens, B.: Evaluation of the Ground Heat Flux Simulated by a Multi-Layer Land Surface Scheme Using High-Quality Observations at Grass Land and Bare Soil, Meteorologische Zeitschrift, 25, 607–620, https://doi.org/10.1127/metz/2016/0537, 2016.

Serafin, S., Adler, B., Cuxart, J., De Wekker, S., Gohm, A., Grisogono, B., Kalthoff, N., Kirshbaum, D., Rotach, M., Schmidli, J., Stiperski, I., Večenaj, Ž., and Zardi, D.: Exchange Processes in the Atmospheric Boundary Layer Over Mountainous Terrain, Atmosphere, 9, 102, https://doi.org/10.3390/atmos9030102, 2018.

Serafin, S., Rotach, M. W., Arpagaus, M., Colfescu, I., Cuxart, J., De Wekker, S. F. J., Evans, M., Grubišić, V., Kalthoff, N., Karl, T., Kirshbaum, D. J., Lehner, M., Mobbs, S., Paci, A., Palazzi, E., Raudzens Bailey, A., Schmidli, J., Wohlfahrt, G., and Zardi, D.: Multi-Scale Transport and Exchange Processes in the Atmosphere over Mountains, innsbruck university press, ISBN 978-3-99106-003-1, https://doi.org/10.15203/99106-003-1, 2020.

Shaw, T. E., Buri, P., McCarthy, M., Miles, E. S., Ayala, Á., and Pellicciotti, F.: The Decaying Near-Surface Boundary Layer of a Retreating Alpine Glacier, Geophysical Research Letters, 50, e2023GL103 043, https://doi.org/10.1029/2023GL103043, 2023.

Shaw, T. E., Miles, E. S., McCarthy, M., Buri, P., Guyennon, N., Salerno, F., Carturan, L., Brock, B., and Pellicciotti, F.: Mountain Glaciers Recouple to Atmospheric Warming over the Twenty-First Century, Nature Climate Change, https://doi.org/10.1038/s41558-025-02449-0, 2025.

Smagorinsky, J.: General Circulation Experiments with the Primitive Equations, Monthly Weather Review, 91, 99–164, https://doi.org/10.1175/1520-0493(1963)091<0099:GCEWTP>2.3.CO;2, 1963.

Strasser, U., Marke, T., Braun, L., Escher-Vetter, H., Juen, I., Kuhn, M., Maussion, F., Mayer, C., Nicholson, L., Niedertscheider, K., Sailer, R., Stötter, J., Weber, M., and Kaser, G.: The Rofental: A High Alpine Research Basin (1890–3770 m a.s.l.) in the Ötztal Alps (Austria) with over 150 Years of Hydrometeorological and Glaciological Observations, Earth System Science Data, 10, 151–171, https://doi.org/10.5194/essd-10-151-2018, 2018.

https://doi.org/10.5194/egusphere-2026-3922
Preprint. Discussion started: 21 July 2026
© Author(s) 2026. CC BY 4.0 License.

UIBK: Weather Station Portal - Station list, https://acinn-data.uibk.ac.at/pages/station-list.html, (last access: 22 June 2026), 2026.

Umek, L., Gohm, A., Haid, M., Ward, H. C., and Rotach, M. W.: Large-eddy Simulation of Foehn–Cold Pool Interactions in the Inn Valley during PIANO IOP 2, Quarterly Journal of the Royal Meteorological Society, 147, 944–982, https://doi.org/10.1002/qj.3954, 2021.

Wagner, J. S., Gohm, A., and Rotach, M. W.: The Impact of Horizontal Model Grid Resolution on the Boundary Layer Structure over an Idealized Valley, Monthly Weather Review, 142, 3446–3465, https://doi.org/10.1175/MWR-D-14-00002.1, 2014.

WGMS: Hintereisferner, Alps, https://wgms.ch/products_ref_glaciers/hintereisferner-alps/, (last access: 22 June 2026), 2026.

Zängl, G., Reinert, D., Rípodas, P., and Baldauf, M.: The ICON (ICOsahedral Non-hydrostatic) Modelling Framework of DWD and MPI-M : Description of the Non-hydrostatic Dynamical Core, Quarterly Journal of the Royal Meteorological Society, 141, 563–579, https://doi.org/10.1002/qj.2378, 2015.

Zängl, G., Reinert, D., and Prill, F.: Grid Refinement in ICON v2.6.4, Geoscientific Model Development, 15, 7153–7176, https://doi.org/10.5194/gmd-15-7153-2022, 2022.

Zardi, D. and Whiteman, C. D.: Diurnal Mountain Wind Systems, in: Mountain Weather Research and Forecasting, edited by Chow, F. K., De Wekker, S. F., and Snyder, B. J., pp. 35–119, Springer Netherlands, Dordrecht, ISBN 978-94-007-4097-6 978-94-007-4098-3, https://doi.org/10.1007/978-94-007-4098-3_2, 2013.